

## Modeling Subtype-Selective Agonists Binding with $\alpha 4\beta 2$ and $\alpha 7$ Nicotinic Acetylcholine Receptors: Effects of Local Binding and Long-Range Electrostatic Interactions

Xiaoqin Huang, Fang Zheng, Xi Chen, Peter A. Crooks, Linda P. Dwoskin, and Chang-Guo Zhan\*

Department of Pharmaceutical Sciences, College of Pharmacy, University of Kentucky, 725 Rose Street, Lexington, Kentucky 40536

Received June 4, 2006

The subtype-selective binding of 14 representative agonists with  $\alpha 4\beta 2$  and  $\alpha 7$  nicotinic acetylcholine receptors (nAChRs) has been studied by performing homology modeling, molecular docking, geometry optimizations, and microscopic and phenomenological binding free energy calculations. All of the computational results demonstrate that the subtype selectivity of the agonists binding with  $\alpha 4\beta 2$  and  $\alpha 7$  nAChRs is affected by both local binding and long-range electrostatic interactions between the receptors and the protonated structures of the agonists. The effects of the long-range electrostatic interactions are mainly due to the distinct difference in the net charge of the ligand-binding domain between the two nAChR subtypes. For the  $\alpha 4\beta 2$ -selective agonists examined, the microscopic binding modes with the  $\alpha 4\beta 2$  nAChR are very similar to the corresponding modes with the  $\alpha 7$  nAChR, and therefore, the subtype selectivity of these agonists binding with  $\alpha 4\beta 2$  and  $\alpha 7$  nAChRs is dominated by the long-range electrostatic interactions. For the  $\alpha 7$ -selective agonists, their microscopic binding modes with the  $\alpha 7$  nAChR are remarkably different from those with the  $\alpha 4\beta 2$  nAChR so that the local binding (including the hydrogen bonding and cation– $\pi$  interactions) with the  $\alpha 7$  nAChR is much stronger than that with the  $\alpha 4\beta 2$  nAChR. The calculated phenomenological binding free energies are in good agreement with available experimental data for the relative binding free energies concerning the subtype selectivity of agonists binding with the two different nAChR subtypes. The fundamental insights obtained in the present study should be valuable for future rational design of potential therapeutic agents targeted to specific nAChR subtypes.

### Introduction

Nicotinic acetylcholine receptors (nAChRs), also known as members of the Cys-loop receptors superfamily, control electrical signaling of fast synaptic transmissions through ligand gating of their membrane spanning channels.<sup>1–12</sup> By modulating many major neurotransmitter systems, these receptors directly mediate a broad range of brain functions, such as learning and memory.<sup>8,9</sup> Abnormal opening and closing of these ligand-gated channels contribute to neurodegenerative disorders, resulting in several kinds of severe diseases, such as Alzheimer's disease, Parkinson's disease, dyskinesias, Tourette's syndrome, schizophrenia, attention deficit disorder, anxiety, and pain, as well as nicotine addiction.<sup>1,3,5–8,11,12</sup> Electrophysiological and functional analyses have revealed that each nAChR structure consists of five protein subunits (see Figure 1), and only the  $\alpha$ -type subunit provides unique contributions to the kinetics of channel gating and ligand binding.<sup>2,3,8,9,12</sup> A total of 12 different subunits (from  $\alpha 2$  to  $\alpha 10$  and from  $\beta 2$  to  $\beta 4$ ) for neuronal nAChRs have been identified, and all of the nAChR protein subunits characterized to date possess a high degree of sequence homology. Of all the nAChR subtypes identified,  $\alpha 4\beta 2$  and  $\alpha 7$  have been recognized as the two major targets mediating the pathology of the above-mentioned diseases, and these subtypes have therefore received considerable attention.<sup>1,6,8,9,12</sup>

Recent pharmacological and structural studies on nAChRs have focused on  $\alpha 4\beta 2$  and  $\alpha 7$  subtypes.<sup>13,14</sup> The  $\alpha 4\beta 2^*$  subtype is the most common subtype and accounts for over 90% of the high-affinity nicotine binding sites in brain.<sup>8,9,13a,b</sup> Activation of  $\alpha 4^*$  subtype receptors is sufficient for nicotine-induced reward, tolerance, and sensitization effects,<sup>13b</sup> and the  $\beta 2$  subunit has been identified immunocytochemically in all dopaminergic

neurons in the ventral tegmental area in the midbrain.<sup>13c,d</sup> The  $\beta 2$ -containing nAChRs exhibit positive interactions with the G proteins including  $G_o\alpha$  or  $\beta\gamma$  subunits, whereas  $\alpha 7$  has no such coupling with any subunit of G proteins.<sup>13e,f</sup> The  $\alpha 7$  nAChR is more directly involved in apoptosis of human lymphocytes and is up-regulated by tyrosine dephosphorylation, and its gating could be altered by amyloid  $\beta_{1-42}$ .<sup>14b,f</sup> The  $\alpha 7$  nAChR has also been used as a typical model system to perform experimental structure–function studies for the entire nAChR family.<sup>14a,c–e</sup> Thus, understanding the common features and differences in selective ligand binding at  $\alpha 4\beta 2$  and  $\alpha 7$  nAChRs is important for the rational design of potential subtype-directed therapeutics.

In the past decades, great efforts, including organic synthesis, structural modifications based on different skeletons of small molecules, and pharmacological testing, have been expended on the design and discovery of lead compounds targeting nAChRs.<sup>15,16</sup> Table 1 is a collection of representatives of the known  $\alpha 4\beta 2$ - or  $\alpha 7$ -specific agonists, including *S*-(–)-nicotine (**1**),<sup>15d</sup> (–)-deschloroepibatidine (**2**),<sup>17</sup> *S*-3-methyl-5-(1-methyl-2-pyrrolidinyl)isoxazole (ABT-418, **3**),<sup>18</sup> (5-pyridyl)-9-azabicyclo[4.2.1]non-2-ene (**4**),<sup>19</sup> 3-(2-*S*-azetidylmethoxy)pyridine (A-85380, **5**),<sup>20</sup> 1,6,7,8,9-tetrahydro-6,10-methano-6*H*-pyrazino[2,3-*h*][3]benzazepine (Varenicline, **6**),<sup>21</sup> 2-methyl-3-(2-*S*-pyrrolidinylmethoxy)pyridine (ABT-089, **7**),<sup>22</sup> *E-N*-methyl-4-(3-pyridinyl)-3-butene-1-amine (TC-2403, **8**),<sup>23</sup> (–)-spiro[1-azabicyclo[2.2.2]octane-3,5'-oxazolidin-2'-one] (ARR-17779, **9**),<sup>24a</sup> *R*-3'-(3-methylbenzo[*b*]thiophen-5-yl)spiro[1-azabicyclo[2,2,2]octane-3,5'-oxazolidin]-2'-one (**10**),<sup>25a</sup> *R*-3'-(5-chlorothiophen-2-yl)spiro-1-azabicyclo[2.2.2]octane-3,5'-[1',3']oxazolidin-2'-one (**11**),<sup>25b</sup> *N*-(3*R*-1-azabicyclo[2.2.2]oct-3-yl)-4-chlorobenzamide hydrochloride (PNU-282987, **12**),<sup>25c</sup> *N*-(3*R*-1-azabicyclo[2.2.2]oct-3-yl)benzofuro[2,3-*c*]pyridine-5-carboxamide (**13**),<sup>25d</sup> and *N*-(3*R*-

\* To whom correspondence should be addressed. Phone: 859-323-3943. Fax: 859-323-3575. E-mail: zhan@uky.edu.

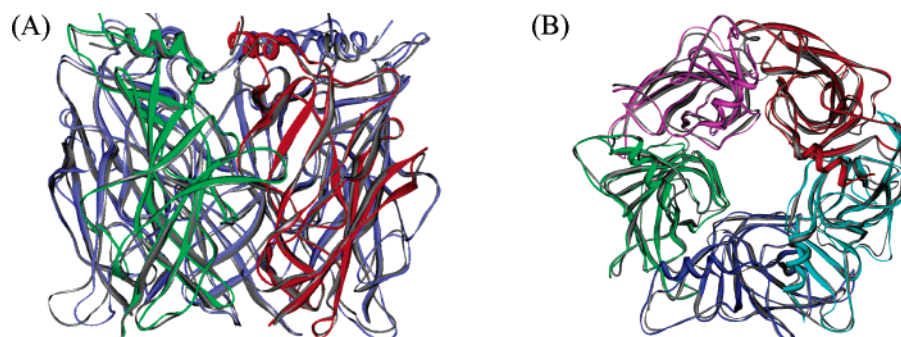


**Figure 1.** Ligand-binding domain (LBD) of the  $\alpha 7$  nAChR modeled in this study (see text for the modeling method). (A) Parallel view along the normal of membrane: one subunit in green, another in red, and the other three in blue. For comparison, the LBD of the  $\alpha 4\beta 2$  nAChR is superimposed and is in gray. (B) Top view of (A) toward the membrane. All five subunits of the  $\alpha 7$  nAChR are shown in different colors, and the  $\alpha 4\beta 2$  nAChR is shown in gray.

1-azabicyclo[2.2.2]oct-3-yl)furo[2,3-*c*]pyridine-5-carboxamide (PHA-543613, **14**).<sup>25d</sup>

Structure–activity relationships established in the literature<sup>15,16</sup> cannot satisfactorily explain the observed binding affinity differences. Generally, it is known that an agonist with a protonable amine moiety (Table 1) can have multiple molecular species coexisting in solution.<sup>26</sup> This generates questions concerning the dominant molecular species for a given ligand binding with a specific receptor. Hence, to fully understand the selective binding of an agonist with different nAChR subtypes, one first needs to know both the detailed three-dimensional (3D) structures of nAChRs and the thermodynamic distribution of the different molecular species of the agonist in solution. The required 3D structures of the nAChRs can be modeled by using the reported crystal structure of the homologous acetylcholine-binding protein (AChBP) as a template,<sup>27</sup> in the absence of a high-resolution X-ray crystal structure of nAChR. Although the recently refined structure of the Torpedo ( $\alpha 2(\beta\delta\gamma)$ ) nAChR at 4 Å resolution has provided fundamental insights into the mechanism underlying channel function,<sup>28</sup> this structure is a modeled structure of the closed channel, and the binding site in this structure is obviously distorted by inter- and intrasubunit interactions. Earlier structural models of  $\alpha 4\beta 2$  and  $\alpha 7$  nAChRs built on the HEPES-bound AChBP structure did not consider the conformational rearrangements occurring during agonist binding;<sup>29</sup> thus, the detailed atomic contacts between nicotine and the receptor are not reliable.<sup>30</sup> Thus far, the agonist-bound AChBP can be used as the most appropriate template to model the ligand-binding domain (LBD) of nAChRs for the purpose of studying receptor–ligand binding.<sup>31</sup> We found no remarkable difference in the binding site between the nicotine-bound *Lymnaea stagnalis* AChBP structure (*L*-AChBP, PDB entry of 1UW6 at 2.2 Å resolution)<sup>27b</sup> and the latest epibatidine-bound *Aplysia* AChBP structure (*A*-AChBP, PDB entry of 2BYQ at 3.4 Å resolution)<sup>31a</sup> because their root-mean-square-deviation (rmsd) was 0.51 Å for the C $\alpha$  atoms within the binding site and 0.55 Å for the corresponding backbone atoms. Hence, the X-ray crystal structure of the nicotine-bound *L*-AChBP<sup>27b</sup> was used as a template to model the LBD of the  $\alpha 4\beta 2$  nAChR in our recent computational studies on  $\alpha 4\beta 2$  nAChR binding with multiple molecular species of **1** and **2**.<sup>26</sup> The modeled structure is consistent with all of the experimental observations reported for  $\alpha 4\beta 2$  nAChRs in the literature and has led us to satisfactorily elucidate the microscopic and phenomenological binding of the  $\alpha 4\beta 2$  nAChR with **1** and **2**.<sup>26</sup> The computational results and analyses also demonstrate that all the molecular species of an agonist (i.e., **1** or **2**) are interchangeable and can quickly achieve a thermodynamic equilibration in solution and at the nAChR binding site. This allows quantification of the

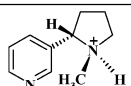
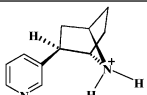
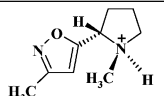
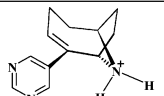
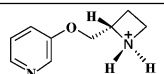
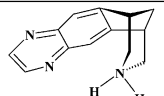
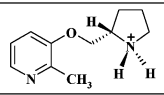
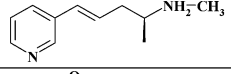
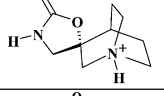
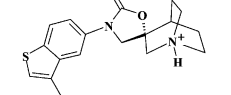
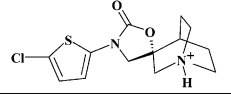
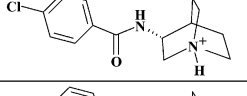
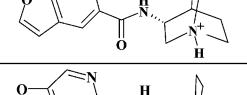
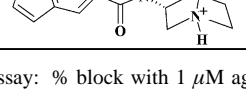
equilibrium concentration distributions of the free ligand species and the corresponding microscopic receptor–ligand binding species, pH dependencies, and their contributions to the phenomenological binding affinity. The predicted equilibrium concentration distributions, pK<sub>a</sub> values, absolute phenomenological binding affinities, and their pH dependence are all in good agreement with available experimental data, suggesting that the computational strategy from the microscopic binding species and affinities to the phenomenological binding affinity is reliable for studying nAChR binding with a ligand.<sup>26</sup>

The general computational strategy of the “from microscopic to phenomenological binding” approach used for studying  $\alpha 4\beta 2$  nAChR binding with **1** and **2** has been extended in the present work to examine the aforementioned crucial question of subtype selectivity for nAChR agonist binding. Specifically, this computational study focuses on understanding how the aforementioned representative agonists (Table 1) bind with  $\alpha 4\beta 2$  and  $\alpha 7$  nAChRs and why these agonists have remarkably different binding affinities with these two important nAChR subtypes. For this purpose, we first modeled the LBD of the  $\alpha 7$  nAChR utilizing a similar approach as that used for the LBD of the  $\alpha 4\beta 2$  nAChR.<sup>26</sup> The modeled structures of the receptors were then used to determine the microscopic receptor–ligand binding structures and to evaluate the phenomenological binding affinities. The determined microscopic binding structures and the calculated binding free energies will provide valuable clues for understanding the selective binding of ligands with different nAChR subtypes and will be useful for future rational design of subtype-selective ligands as possible therapeutic treatments for the aforementioned diseases.

## Computational Methods

**Homology Modeling of the LBD of the  $\alpha 7$  nAChR.** The LBD of the  $\alpha 7$  nAChR was modeled in a similar way (including use of the same template, i.e., the X-ray crystal structure of nicotine-bound *L*-AChBP, PDB entry of 1UW6 at 2.2 Å resolution) as our previous modeling of the LBD of the  $\alpha 4\beta 2$  nAChR.<sup>26</sup> Briefly, the sequence alignment was generated by ClusterW with the Blosum scoring function<sup>32,33</sup> and all of the five subunits were modeled simultaneously in order to maintain complementarity between these subunits at the interface. The best alignment was selected according to both the alignment score and the reciprocal position of the conserved residues. These include the conserved GWS sequence (in which Trp148 of the  $\alpha 7$  nAChR corresponded to Trp143 of the *L*-AChBP) and the C loop (containing Cys189 and Cys190) between  $\beta$ -strands 9 and 10 of the  $\alpha 7$  nAChR. The coordinates of the conserved regions were transformed directly from the template structure (i.e., the X-ray crystal structure of the *L*-AChBP<sup>27b</sup>),

**Table 1.** Protonated Molecular Structures of Some Representative Agonists for  $\alpha 4\beta 2$  and  $\alpha 7$  nAChRs, along with Their Experimental Binding Affinities ( $K_d$ ) and Selectivities ( $K_{d(\alpha 7)}/K_{d(\alpha 4\beta 2)}$ )

Compound	Molecular structure	$K_d$ (nM)		$K_{d(\alpha 7)}/K_{d(\alpha 4\beta 2)}$	Ref.
		$\alpha 4\beta 2$	$\alpha 7$		
1		1.10	1000	909	15
2		0.020	109	5450	17
3		52.9±12.9	>10000	>189	18
4		2.45	1706±223	696	19a
5		0.015	17	1133	20a
6		0.06	322	5366	21
7		39	>10000	>256	22
8		26.0	36000	1384	23a
9		16000	92	1/174	24
10		>10000	3.0	<1/3333	25a
11		1800	9	1/200	25b
12		14% <sup>a</sup>	24±8	<1/148	25c
13		5% <sup>a</sup>	1.6±0.3	<1/6250	25d
14		13% <sup>a</sup>	8.8±1.3	<1/437	25d

<sup>a</sup> From rat brain homogenate binding assay: % block with 1  $\mu$ M agonist.

whereas the nonequivalent residues were mutated from the template to the corresponding ones of the  $\alpha 7$  nAChR. The side chains of these nonconserved residues were relaxed by using the Homology module of InsightII (version 2000, Accelrys, Inc., San Diego, CA) in order to remove possible steric overlap or hindrance with the neighboring conserved residues.

The other steps of model construction were identical to those reported previously for the  $\alpha 4\beta 2$  nAChR;<sup>26</sup> the standard protonation states in the physiological environment (pH ~7.4) were set to all ionizable residues, and the proton was set on  $N_{\epsilon 2}$  atoms in His62 and His104 and on  $N_{\delta 1}$  in His114. The 3D

model was energy-minimized using the Sander module of the Amber7 program suite<sup>34</sup> with a nonbonded cutoff of 10 Å and a conjugate gradient minimization method. Energy minimization was performed first for 1000 steps with the backbone atoms fixed while the side chain atoms were relaxed in the gas phase and then for another 1000 steps with the side chain atoms constrained in order to relax the backbone. After each of these stages was finished, the receptor structure was visually checked to ensure that there was no significant distortion during the energy-minimization processes, checking especially for any possible distortion at the corresponding binding site. After

several rounds of these partial energy-minimization runs, the convergence criterion of  $0.01 \text{ kcal mol}^{-1} \text{ \AA}^{-1}$  was achieved in a full energy minimization. The fully energy-minimized structure was carefully checked to make sure that the overall structure of the final model was not significantly different from that of the initial model and the template. Finally, the modeled structure was validated by using PROCHECK and WHATIF programs.<sup>35</sup>

**Molecular Dynamics Simulation.** In order to determine how stable the LBD structures of  $\alpha 4\beta 2$  and  $\alpha 7$  nAChRs are, molecular dynamics (MD) simulations were performed on both of the modeled receptors. Each of the LBD structures was solvated in a rectangular box of TIP3P water molecules<sup>36</sup> with a minimum solute–wall distance of  $10 \text{ \AA}$ . Different numbers of counterions (67  $\text{Na}^+$  ions and 30  $\text{Cl}^-$  ions for the  $\alpha 4\beta 2$  nAChR; 50  $\text{Na}^+$  ions and 30  $\text{Cl}^-$  ions for the  $\alpha 7$  nAChR) were randomly swapped with water molecules. These ion concentrations, when combined with the different net charges (i.e.,  $-37e$  for the LBD of the  $\alpha 4\beta 2$  nAChR and  $-20e$  for the LBD of the  $\alpha 7$  nAChR), produced neutral systems that closely mimic the physiological conditions of  $0.10 \text{ M Na}^+$  and  $0.05 \text{ M Cl}^-$  ions. The total number of atoms of the MD-simulated system was 119 925 (including 33 903 water molecules) for the solvated LBD of the  $\alpha 4\beta 2$  nAChR and was 124 502 (including 35 274 water molecules) for the solvated LBD of the  $\alpha 7$  nAChR.

The MD simulations were performed by using the Sander module of Amber<sup>734</sup> in a manner similar to the procedures we used for the other protein–ligand systems.<sup>37</sup> The solvated system was energy-minimized prior to the MD simulation. The energy minimization was performed first on the water molecules and  $\text{Na}^+$  and  $\text{Cl}^-$  ions and then on the protein atoms by using the conjugate-gradient energy minimization method, each for 6000 steps. To avoid possible aggregation of vacuum bubbles and small gaps at the edges of the box due to solvent packing, a  $1.2 \text{ ps}$  MD equilibration at the *NVT* ensemble was performed. Subsequently, the whole system was energy-minimized again for 6000 steps, while the backbone of the protein was constrained. This system was then gradually heated to  $300 \text{ K}$  by the weak-coupling method and equilibrated for about  $37 \text{ ps}$ .<sup>38</sup> Throughout the MD simulations, a  $10 \text{ \AA}$  nonbonded interaction cutoff was used and the nonbonded list was updated every 1000 steps. The particle mesh Ewald (PME) method<sup>39</sup> was applied to treat long-range electrostatic interactions. The lengths of bonds involving hydrogen atoms were fixed with the SHAKE algorithm,<sup>40</sup> enabling the use of a  $2 \text{ fs}$  time step to integrate the equations of motion. Finally, each production MD was kept running for longer than  $13 \text{ ns}$  with a periodic boundary condition in the *NTP* ensemble at  $T = 300 \text{ K}$  with Berendsen temperature coupling<sup>38</sup> and at  $P = 1 \text{ atm}$  with isotropic molecule-based scaling.<sup>38</sup>

**First-Principles Electronic Structure Calculation.** Geometries of the molecular species of the agonists utilized in this study were fully optimized by using density functional theory (DFT) with Becke's three-parameter hybrid exchange function and the Lee–Yang–Parr correlation function<sup>41</sup> (B3LYP) in combination with the 6-31+G(d) basis set. Vibrational frequency calculations were carried out to confirm the optimized stable molecular structures and to perform zero-point vibration and thermal corrections to the Gibbs free energies. The geometries optimized at the B3LYP/6-31+G(d) level were used to carry out second-order Møller–Plesset (MP2) single-point energy calculations with the 6-31++G(d,p) basis set. All these electronic structure calculations in the gas phase were performed by using the Gaussian 03 program.<sup>42</sup>

The solvent shifts of the Gibbs free energies were calculated by performing self-consistent reaction field (SCRF) calculations on the geometries optimized at the B3LYP/6-31+G(d) level in the gas phase. The SCRF method used in the calculations is our recently developed GAMESS implementation<sup>43</sup> of the surface and volume polarization for electrostatic interactions (SVPE).<sup>44</sup> The SVPE model is also known as the fully polarizable continuum model (FPCM)<sup>45,46</sup> because it fully accounts for both surface and volume polarization effects in the SCRF calculation. In other SCRF implementations, volume polarization effects are ignored or approximately modeled by modifying the surface polarization charge distribution through a simulation and/or charge renormalization,<sup>47–55</sup> or the solute charge distribution is simply represented by a set of point charges at the solute nuclei.<sup>56,57</sup> Since the solute cavity surface is defined as a solute electron charge isodensity contour determined self-consistently during the SVPE iteration process, the SVPE results, converged to the exact solution of Poisson's equation with a given numerical tolerance, depend only on the contour value at a given dielectric constant and a certain quantum chemical calculation level.<sup>44a</sup> This single parameter value has been determined to be  $0.001 \text{ au}$  based on an extensive calibration study.<sup>44b</sup> Accordingly, the default  $0.001 \text{ au}$  contour was used in this study. The free energy of a molecular species in aqueous solution was taken as the sum of the free energy calculated at the MP2/6-31++G(d,p)//B3LYP/6-31+G(d) level in the gas phase and the corresponding solvent shift determined by the SVPE calculation at the HF/6-31+G(d) level.

On the basis of the calculated Gibbs free energies and the previously determined absolute free energy of the proton ( $\text{H}^+$ ) in aqueous solution, i.e.,  $\Delta G_{\text{hyd}}^{298}(\text{H}^+) = -262.4 \text{ kcal/mol}$ ,<sup>58–61</sup> we were able to evaluate the free energy change ( $\Delta G_a$ ) of a given deprotonation process and therefore to estimate the corresponding  $\text{p}K_a$  via  $\text{p}K_a = \Delta G_a / (2.303RT)$ . This SVPE-based first-principles electronic structure approach has been used previously to solve a variety of chemical and biochemical problems in solution, and the predicted activation free energies for chemical reactions,  $\text{p}K_a$  values, thermodynamic properties, etc. are all in good agreement with the available experimental data.<sup>45,46</sup>

**Molecular Docking and Optimization of the Microscopic Binding Mode.** On the basis of the LBD model of the  $\alpha 7$  nAChR obtained in the present study and the LBD model of the  $\alpha 4\beta 2$  nAChR obtained in an earlier study,<sup>26</sup> each of the considered agonist structures was docked into the binding sites of  $\alpha 4\beta 2$  and  $\alpha 7$  nAChRs using the AutoDock 3.0.5 program.<sup>62</sup> The hydrogen-bonding energies were calculated by using a reparametrized equation (see below). The docking and subsequent binding free energy calculations were performed in a similar manner as previously reported<sup>26</sup> for the  $\alpha 4\beta 2$  nAChR binding with **1** and **2**. Briefly, the atomic charges of all molecular species were the restrained electrostatic potential (RESP) charges determined using the standard RESP procedure implemented in the Antechamber module of the Amber 7 program<sup>34</sup> following the electronic structure and electrostatic potential calculations. During the docking process, a conformational search was performed using the Solis and Wets local search method,<sup>63</sup> and the Lamarkian genetic algorithm (LGA)<sup>62</sup> was applied to deal with the receptor–ligand interactions. Among a series of docking parameters, the grid size was set to  $60 \times 60 \times 60$  and the grid space used was the default value of  $0.375 \text{ \AA}$ . The docked receptor–ligand complex structures from this first round of docking were ranked according to the criteria of interacting energy combined with geometric matching quality.

	Principal (+)	Complementary (-)	
A-AChBP	-- <b>YS</b> - <b>GSWVY</b> - <b>HYS</b> <b>CCPEPY</b> ID-	- <b>YEQQR</b> - <b>I</b> AVVTGDG <b>SV</b> <b>MFIP</b> -	A-AChBP
L-AChBP	-- <b>YN</b> - <b>GSWTH</b> - <b>TYS</b> <b>CCPEAYE</b> D-	- <b>FWQQT</b> T-LARVVSDG <b>EV</b> <b>LYMP</b> -	L-AChBP
	--91---147--188-191--195-	--53-----109-----117119	
$\alpha 4$	-- <b>YN</b> - <b>GSWTY</b> - <b>KYE</b> <b>CCAEI</b> YPD-	- <b>V</b> LTQE- <b>NAV</b> VS <b>YDGS</b> <b>IFWLP</b> -	$\beta 2$
$\alpha 7$	-- <b>YN</b> - <b>GSWSY</b> - <b>FYE</b> <b>CKEPE</b> YPD-	- <b>I</b> WLQMS- <b>N</b> VLV <b>NASGH</b> <b>CQYLP</b> -	$\alpha 7$
	--92---148--187-190--194-	--54-----108-----116118	
$\alpha 4$	-- <b>YN</b> - <b>GSWTY</b> - <b>KYE</b> <b>CCAEI</b> YPD-	- <b>V</b> WLKQE- <b>K</b> AI <b>VKSS</b> GT <b>VS</b> <b>WTP</b> -	$\beta 3$
$\alpha 3$	-- <b>YN</b> - <b>GSWSY</b> - <b>KYN</b> <b>CCEEI</b> YQD-	- <b>V</b> LTQE- <b>NAV</b> VS <b>YDGS</b> <b>IFWLP</b> -	$\beta 2$
$\alpha 3$	-- <b>YN</b> - <b>GSWSY</b> - <b>KYE</b> <b>CCEEI</b> YQD-	- <b>I</b> WLKQE- <b>N</b> VI <b>VR</b> S <b>NGS</b> <b>IQWLP</b> -	$\beta 4$
$\alpha 6$	-- <b>YN</b> - <b>GSWTY</b> - <b>KYN</b> <b>CCEEI</b> YTD-	- <b>V</b> WLKQE- <b>K</b> AI <b>VKSS</b> GT <b>VS</b> <b>WTP</b> -	$\beta 3$
$\alpha 6$	-- <b>YN</b> - <b>GSWTY</b> - <b>KYN</b> <b>CCEEI</b> YTD-	- <b>I</b> WLKQE- <b>N</b> VI <b>VR</b> S <b>NGS</b> <b>IQWLP</b> -	$\beta 4$

**Figure 2.** Sequence alignment of the amino acid residues around the agonist binding site for the subunits of  $\alpha 4\beta 2$ ,  $\alpha 7$ , and other nAChR subtypes with the reported acetylcholine binding protein (AChBP) from *Aplysia californica* (A-AChBP)<sup>27b</sup> and *Lymnaea stagnalis* (L-AChBP).<sup>31a</sup> The binding pocket is composed of the colored residues; red ones are in the aromatic cage. Residues in the binding site that are different in the various subtypes are in blue, while the typical disulfide is colored in pink. The binding site is decomposed as the principal (+)-side and complementary (-)-side according to the convention used for the X-ray crystal structure of L-AChBP.<sup>27b</sup> The sequence numbers are labeled for both L-AChBP and  $\alpha 7$  nAChR.

Because molecular docking with the AutoDock 3.0.5 program could not consider structural flexibility of the binding site, we further performed energy minimization and conformational relaxation for these initial complexes as follows. By use of the Sander module of the Amber 7 program,<sup>34</sup> 1000 steps of energy minimization were performed first with the backbone and the ligand fixed and then for the whole complex system. This was followed by  $\sim 3.8$  ps MD simulation in the NTV ensemble with the backbone constrained and ended with the same minimization process as was performed prior to the MD simulation.

The second round of molecular docking was performed in situ on the energy-minimized complexes, and for each molecular species binding with a receptor, the final microscopic binding complex was identified from 10 candidates of the docked structures, according to the extent of fit between the ligand and receptor and the interacting energy score determined initially by the AutoDock 3.0.5 program.<sup>62</sup> The microscopic binding structure with the best score was subjected to a final, fully relaxed energy minimization with the Sander module of the Amber 7 program.

**Calculation of Microscopic Binding Free Energy.** On the basis of the final energy-minimized structures, the microscopic binding free energy for each molecular species binding with either  $\alpha 4\beta 2$  or  $\alpha 7$  nAChR was estimated by using a slightly modified binding free energy functional form:

$$\Delta G_{\text{bind}} = \alpha(\Delta G_{\text{AD}} - E_0) + \Delta G_{\text{HB}} + \Delta G_{\text{LRE}} \quad (1)$$

In eq 1,  $\Delta G_{\text{AD}}$  is the binding free energy calculated using the standard binding free energy functional form implemented in the AutoDock 3.0.5 program<sup>62</sup> but with the contribution from hydrogen bonding to the binding free energy removed. The hydrogen-bonding energy was excluded in the calculation of  $\Delta G_{\text{AD}}$  because we noted that the standard binding free energy functional form implemented in the program generally underestimated the hydrogen-bonding energy. Thus, we needed to reparametrize the parameters used in the hydrogen-bonding energy calculation. We also noted that the long-range electrostatic interactions between the ligand and receptor were underestimated considerably in the calculations with the standard binding free energy functional form implemented in the AutoDock 3.0.5 program.<sup>62</sup> Hence, we also added an additional correction of binding free energy reflecting the underestimated long-range electrostatic interactions.  $\Delta G_{\text{HB}}$  is the contribution from the receptor–ligand hydrogen bonding to the binding free

energy.  $\Delta G_{\text{LRE}}$  is the binding free energy correction associated with the long-range electrostatic interactions between all of the ligand atoms and all of the receptor atoms outside a  $22.5 \text{ \AA} \times 22.5 \text{ \AA} \times 22.5 \text{ \AA}$  box (corresponding to the  $60 \times 60 \times 60$  grid) centered at the mass center of the ligand.  $\Delta G_{\text{HB}}$  and  $\Delta G_{\text{LRE}}$  are determined by using the following equations:

$$\Delta G_{\text{HB}} = \sum_{i=1}^N \left( \frac{\beta_{12}}{R_i^{12}} - \frac{\beta_{10}}{R_i^{10}} \right) = \beta_{12} \sum_{i=1}^N \frac{1}{R_i^{12}} - \beta_{10} \sum_{i=1}^N \frac{1}{R_i^{10}} \quad (2)$$

in which  $R_i$  is the H $\cdots$ O distance for the  $i$ th hydrogen bond between the ligand and receptor;

$$\Delta G_{\text{LRE}} = \lambda \sum_{i \in R} \sum_{j \in L} \frac{q_i q_j}{\epsilon(R_{ij}) R_{ij}} \quad (3)$$

in which  $R_{ij}$  is the internuclear distance between the  $i$ th atom (with a point charge of  $q_i$ ) of the receptor and the  $j$ th atom (with a point charge of  $q_j$ ) of the ligand.  $\epsilon(R_{ij})$  is the distance-dependent dielectric constant determined by using the same function<sup>64</sup> implemented in the AutoDock 3.0.5 program.<sup>62</sup>

In eqs 1–3,  $\alpha$ ,  $E_0$ ,  $\beta_{12}$ ,  $\beta_{10}$ , and  $\lambda$  are the universal empirical parameters to be calibrated.

Most of the MD simulations were performed on the HP supercomputers (Superdome SDX and Linux cluster XC) at the University of Kentucky Center for Computational Sciences and at the Pacific Northwest National Laboratory. The other computations were carried out on SGI Fuel workstations and on a 34-processor IBM x335 Linux cluster in our laboratory.

## Results and Discussion

**(1) Structural Models of  $\alpha 4\beta 2$  and  $\alpha 7$  nAChRs.** The sequence alignment (see Figure 2) revealed that most of the amino acid residues within the binding sites of the  $\alpha 7$  and  $\alpha 4\beta 2$  nAChRs are the same or quite similar. The similar residues form a typical aromatic cage<sup>27b</sup> at the bottom of the binding pocket, including Trp148, Tyr92, Tyr187, Tyr194, and the disulfide at positions 189 and 190 of the C loop of the principal (+)-binding side and Trp54 of the complementary (-)-binding side. Note that all of the amino acid numbers given here are for the  $\alpha 7$  nAChR. The corresponding numbering of the  $\alpha 4\beta 2$  nAChR is slightly different. For example, Trp54 at the complementary (-)-side in the  $\alpha 7$  nAChR becomes  $\beta$ Trp53 (i.e., Trp53 of the  $\beta 2$

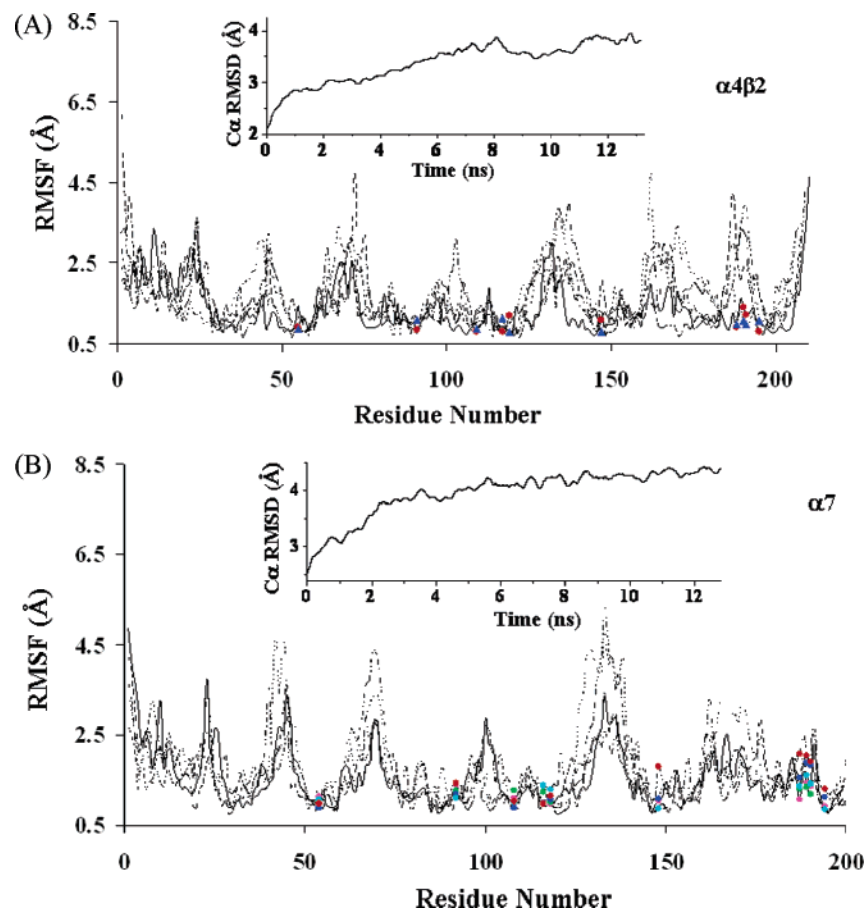


**Figure 3.** Residue-based fluctuations during the MD simulations in which all five subunits are represented sequentially in different line styles. Pasted also are the plots of the C $\alpha$  rmsd of the whole system versus the simulation time. (A) The LBD of the  $\alpha 4\beta 2$  nAChR, where the dots represent the rmsf values for the residues at the binding sites (red for the first binding site and blue for the second binding site). (B) The LBD of the  $\alpha 7$  nAChR, where the five different colors refer to the five different binding sites.

subunit)) in the  $\alpha 4\beta 2$  nAChR. A major structural difference between  $\alpha 7$  and  $\alpha 4\beta 2$  nAChRs exists in the complementary side. There is a hydrophilic amino acid residue Gln116 of  $\alpha 7$ , which corresponds to an aromatic residue  $\beta$ Phe117 of  $\alpha 4\beta 2$ . This major structural difference could be responsible for the subtype-selective ligand binding with these two nAChR subtypes if a ligand is bulky enough to fill the binding pocket. Such a structural difference was not well appreciated in previous structure–function studies.<sup>14,28–30,65,66</sup>

Through careful inspection of the optimized 3D structure of the LBD of the  $\alpha 7$  nAChR (Figure 1), we noted that the modeled LBD structure of the  $\alpha 7$  nAChR is consistent with all of the general structural features known for both the AChBP and nAChRs.<sup>2,3,4,9,14,27–29,31</sup> Our 3D model obtained for the  $\alpha 7$  nAChR also agrees well with other recently reported 3D models of nAChRs.<sup>30</sup> The homo-oligomer with a 5-fold axis of the  $\alpha 7$  nAChR is similar to the topological arrangement found in the X-ray crystal structures of the AChBP,<sup>27,28</sup> in the recently refined structure of the ( $\alpha$ )2( $\beta\gamma\delta$ ) nAChR,<sup>28</sup> and also in our recently reported  $\alpha 4\beta 2$  nAChR model (Figure 1).<sup>26</sup> The corresponding aromatic cage at the interface of two neighboring subunits, of which one must be the  $\alpha$  type, could serve as a capture area for cationic ligand binding in light of previous experimental and modeling studies of all the nAChR subtypes.<sup>2,3,4,9,14,29,30</sup> Starting from these homologies, the dynamic properties of the LBDs of these two receptor subtypes (i.e.,  $\alpha 4\beta 2$  and  $\alpha 7$  nAChRs) exhibit differences to some extent but had enough overall similarity during the MD simulations (Figures 3 and 4).

As seen in Figure 3, the root-mean-square deviation (rmsd) of C $\alpha$  atoms fluctuated over 4.0 Å during the simulation processes. The rmsd for the  $\alpha 7$  nAChR from the initial structure (Figure 3B) is slightly larger than that for the  $\alpha 4\beta 2$  nAChR (Figure 3A). Large root-mean-square fluctuations (rmsf values) can be seen for several regions, including not only the N-terminal and the C-terminal but also some local regions without regular secondary structures. Interestingly, all the residues composing the binding sites (colored residues in Figures 2 and 3) retained very small rmsf values during the MD simulations. The Trp residues at positions 54 and 148 have much smaller fluctuations compared with the other binding site residues (Figures 3 and 4). The relative stability of these Trp residues can be illustrated also by the critical distance of each site from the C $\alpha$  of Trp148 for  $\alpha 7$  (or  $\alpha$ Trp147 for  $\alpha 4\beta 2$ ) to the geometric center of the aromatic cage (composed of  $\alpha$ Tyr91,  $\alpha$ Trp147,  $\alpha$ Tyr188,  $\alpha$ Tyr195, and  $\beta$ Trp53 for  $\alpha 4\beta 2$  or Tyr92, Trp148, Tyr187, and Tyr194 of the principal side and Trp54 of the complementary side for  $\alpha 7$ ). As shown in Figure 4, this distance fluctuates within 1 Å for most sites. The fluctuations for the fifth site at the interface of subunits E and A (site EA) of the  $\alpha 7$  nAChR are larger than the others (as is also seen from the rmsf in Figure 3 and the distance parameters in Figure 4), indicating the unbalanced motions among different subunits even for this symmetric nAChR subtype ( $\alpha 7$ ), needless to say the unbalanced motions for  $\alpha 4\beta 2$  or other hetero-oligomeric nAChRs. Similar asymmetric motions have been reported in other computational modeling and simulation studies on  $\alpha 7$  and other nAChRs.<sup>28,30,65,66</sup>

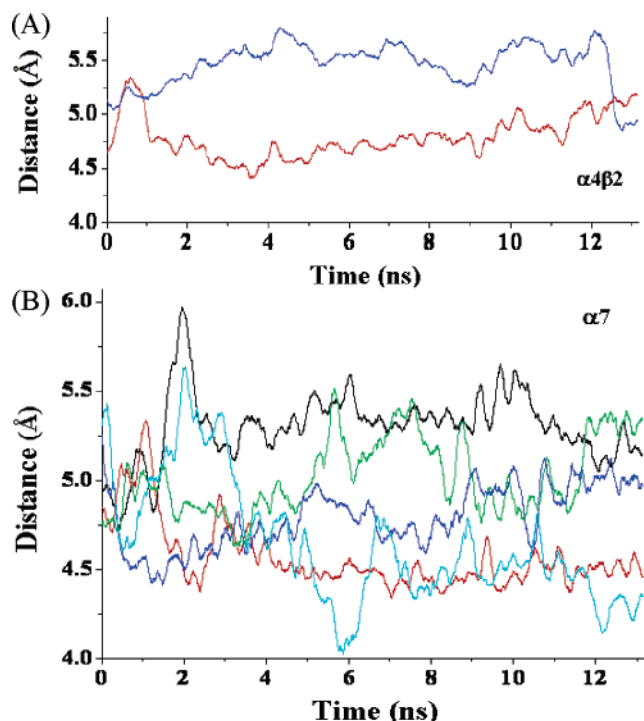


**Figure 4.** Evolution of distances from the geometric center of the aromatic cage to the C $\alpha$  of conserved residue  $\alpha$ Trp147 ( $\alpha 4\beta 2$ ) or Trp148 ( $\alpha 7$ ) during the MD simulation. (A) The LBD of the  $\alpha 4\beta 2$  nAChR, where the aromatic cage is composed of  $\alpha$ Tyr91,  $\alpha$ Trp147,  $\alpha$ Tyr188,  $\alpha$ Tyr195, and  $\beta$ Trp53. Red refers to the first binding site and blue to the second binding site. (B) The LBD of the  $\alpha 7$  nAChR, where the aromatic cage is formed by Tyr92, Trp148, Tyr187, Tyr194, and Trp54 from the next subunits. Five different colors are used for five different binding sites.

**(2) Microscopic Binding Structures.** We examined microscopic binding of  $\alpha 4\beta 2$  and  $\alpha 7$  nAChRs with both the protonated and deprotonated molecular species for each agonist under consideration. Here, we only discuss the binding with the protonated molecular species because the contributions of the binding with the corresponding deprotonated molecular species to the phenomenological binding is negligible for all of the agonists considered. Some representative microscopic binding structures are depicted in Figures 5 and 6; additional information about the microscopic binding structures is provided as Supporting Information (Figures S1–S13). A survey of

Figures 5 and 6 and other figures in Supporting Information reveals that all of the microscopic binding structures are featured with some hydrogen bonds (H-bonds) and/or cation– $\pi$  interactions. The binding modes for **5** and **7** are different from those for **1** and **4** (see Figures S1–S13 in Supporting Information). The distances between the cationic head and the six-membered ring in **5** and **7** are significantly longer than those in **1** and **4**. As a result, the cationic heads of **5** and **7** stay in the binding site more deeply than that of **1** and **4**, as seen in Figures S1A, S4, S5, and S7 of the Supporting Information. This is why the cationic heads of **5** and **7** can also form an additional H-bond with Tyr91. The bulk size of the cationic head of **5** is the smallest, allowing the cationic head of **5** to form H-bonds with both Tyr91 and Trp147 simultaneously. The bulk size of the cationic head of **7** is also very small. However, the methyl group on the six-membered ring of **7** would be too close to the disulfide bond between Cys189 and Cys190 if **7** stayed in exactly the same orientation as **5**; the methyl group significantly affects the binding mode. Thus, the two H-bonds of **7** with Tyr91 and Trp147 are all significantly weaker than those of **5** with Tyr91 and Trp147, as seen from the distances indicated in Figures S5 and S7 of the Supporting Information. The bulk size of the cationic head of **4** is too large to form H-bonds with both Tyr91 and Trp147 simultaneously.

Each of the  $\alpha 4\beta 2$ -specific agonists, including **1–8**, binds with  $\alpha 4\beta 2$  and  $\alpha 7$  nAChRs in a similar way. However, each of the  $\alpha 7$ -specific agonists, including **9** and its derivatives (i.e., **10** and **11**) and **12** and its analogues (i.e., **13** and **14**), binds with  $\alpha 4\beta 2$  and  $\alpha 7$  nAChRs in remarkably different ways; their local binding with the  $\alpha 7$  nAChR is always much stronger than that with the  $\alpha 4\beta 2$  nAChR. In particular, **12** and its analogues (i.e., **13** and **14**) form strong hydrogen bonds and cation– $\pi$  interactions with the  $\alpha 7$  nAChR, whereas **9** and its derivatives **10** and **11** not only directly form hydrogen bonds with the  $\alpha 7$  nAChR but also have a hydrogen-bonding network with the  $\alpha 7$  nAChR through solvent water molecules.

Especially, for **9** (and its derivatives **10** and **11**), the relatively large bulky size of the cationic head of **9** makes it hard to fit into the aromatic cage in the binding site of the  $\alpha 4\beta 2$  nAChR. As a result, the N–H $\cdots$ O hydrogen bonding between the cationic head of **9** and the backbone carbonyl oxygen of  $\alpha$ Trp147 is expected to be weakened considerably, with the H $\cdots$ O distance as long as 2.36 Å. On the other hand, there exists an N–H $\cdots$ O hydrogen bond between the –NH group on the

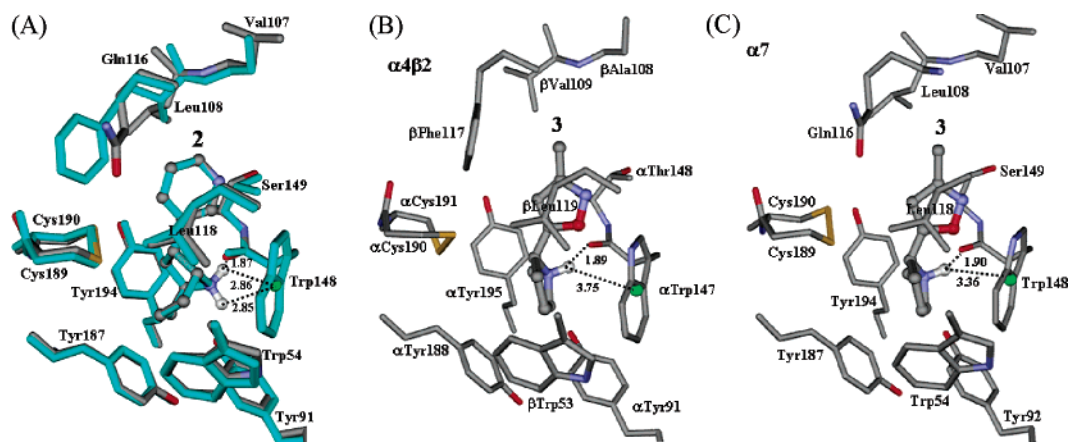


**Figure 5.** (A) Molecular interactions between **2** and the  $\alpha 7$  nAChR. Residues of the receptor are labeled and shown in stick form, whereas the ligand is in ball-and-stick form. Both the hydrogen bonding (HB) and the cation– $\pi$  interactions between the protons of **2** and the aromatic Trp148 of  $\alpha 7$  nAChR are represented by the dashed lines. Distances are labeled for these typical interactions. The corresponding complex of **2** binding with the  $\alpha 4\beta 2$  nAChR is superimposed and colored in cyan but not labeled. (B) Similar view of interactions of **3** with the  $\alpha 4\beta 2$  nAChR. (C) **3** binding with the  $\alpha 7$  nAChR.

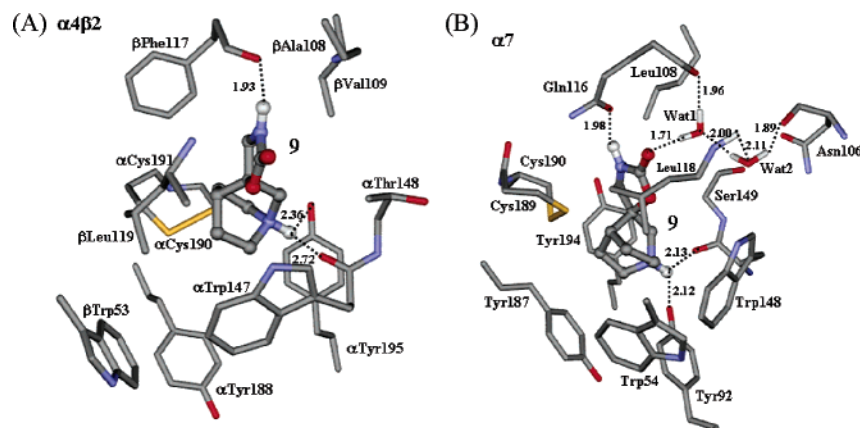


**Figure 6.** (A) Compound **9** binding with the  $\alpha 4\beta 2$  nAChR. The protons at the cationic head of **9** are weakly hydrogen-bonded with both the carbonyl oxygen on the backbone of Trp147 and the hydroxyl oxygen on the side chain of Tyr195 of the  $\alpha 4$  subunit, and the  $-NH$  group at the other end of **9** forms a hydrogen bond with the carbonyl oxygen on the backbone of Phe117 of the  $\beta 2$  subunit. (B) **9** binding with the  $\alpha 7$  nAChR. The proton on the cationic head forms hydrogen bonds with both the carbonyl oxygen on the backbone of Trp148 and the hydroxyl group on the side chain of Tyr92. The  $-NH$  group at the other end of **9** has hydrogen bonding with the carbonyl oxygen on the side chain of Gln116. The water molecule (Wat1) bridges the carbonyl oxygen near the  $-NH$  group of **9** with the carbonyl oxygen on the backbone of Gln116 and another water molecule (Wat2).

five-membered ring of **9** and the backbone carbonyl oxygen of  $\beta$ Phe117 at an  $H\cdots O$  distance of 1.93 Å. The microscopic binding mode of **9** binding with the  $\alpha 7$  nAChR is significantly different from that with the  $\alpha 4\beta 2$  nAChR. Our initial docking without explicitly accounting for any solvent water molecule in the binding site revealed that for **9** binding with  $\alpha 7$  nAChR, the  $-NH$  group on the five-membered ring of **9** could potentially form a  $N-H\cdots O$  hydrogen bond with the carbonyl oxygen of the Gln116 side chain. This is remarkably different from the above-mentioned  $N-H\cdots O$  hydrogen bond between the  $-NH$  group on the five-membered ring of **9** and the backbone carbonyl oxygen of  $\beta$ Phe117 for **9** binding with the  $\alpha 4\beta 2$  nAChR. We further noted a large gap between the carbonyl oxygen of **9** and the backbone carbonyl oxygen of Gln116. We also noted that the backbone carbonyl group of Gln116 and other residues nearby provide a hydrophilic environment that could accommodate some solvent water molecules. Hence, the best possible binding of **9** with the  $\alpha 7$  nAChR could be obtained when the large gap between the carbonyl group of **9** and the binding site of the  $\alpha 7$  nAChR is filled by water molecules. Such a hypothesis is supported conceptually by the fact that a water molecule was found in the X-ray crystal structure of the nicotine-bound AChBP,<sup>27b</sup> although the computational modeling in our recently reported work (with the  $\alpha 4\beta 2$  nAChR)<sup>26</sup> and in the present work (with the  $\alpha 7$  nAChR; results not shown) indicated that the water molecule will leave when the AChBP was replaced by  $\alpha 4\beta 2$  nAChR (see Figure S1 of the Supporting Information). In the X-ray crystal structure of nicotine-bound AChBP, the water molecule bridged the pyridine nitrogen of nicotine with the carbonyl oxygen at the backbone of Leu102 and the  $-NH$  group of Met114 in the binding site. This water bridge was thought to enhance the binding or stabilize the receptor–ligand binding complex.<sup>27b</sup> Hence, we used two water molecules to fill the similar gap positions at the binding site of the  $\alpha 7$  nAChR. This new structural model was energy-minimized prior to the molecular docking of **9** in the second round. Explicit consideration of these two water molecules led to a very stable microscopic structure of **9** binding with the  $\alpha 7$  nAChR (Figure 6B).

As seen in Figure 6B, the favorable binding structure includes three  $N-H\cdots O$  hydrogen bonds between **9** and the backbone carbonyl oxygen of Trp148, the hydroxyl oxygen of the Tyr92 side chain, and the carbonyl oxygen of the Gln116 side chain

of the  $\alpha 7$  nAChR. The  $H\cdots O$  distances for these three hydrogen bonds are 2.13, 2.12, and 1.98 Å for the hydrogen bonds with Trp148, Tyr92, and Gln116, respectively. In addition, the carbonyl oxygen of **9** has a strong  $O-H\cdots O$  hydrogen bond with one of the explicitly considered water molecule (Wat1). Wat1 effectively bridges the carbonyl oxygen of **9** with the backbone carbonyl oxygen of Gln116 through a hydrogen-bonding network. The second water molecule (Wat2) forms a hydrogen bond with Wat1 and two other hydrogen bonds with the receptor. Thus, the two water molecules are involved in a total of five hydrogen bonds in the binding pocket. This microscopic binding mode is expected to be very stable. We also carefully considered whether the  $\alpha 4\beta 2$  nAChR can also accommodate water molecules near  $\beta$ Phe117 in the binding site to form a hydrogen-bonding network similar to that in the  $\alpha 7$  nAChR binding site. We noted that the corresponding part of the binding pocket near  $\beta$ Phe117 is much smaller and is hydrophobic and therefore cannot accommodate water molecules.

**(3) Microscopic and Phenomenological Binding Free Energies.** On the basis of the microscopic binding structures discussed above, the microscopic binding free energies ( $\Delta G_{\text{bind}}$ ) were calculated using eqs 1–3. The empirical parameters, i.e.,  $\alpha$ ,  $E_0$ ,  $\beta_{12}$ ,  $\beta_{10}$ , and  $\lambda$ , used in the equations were calibrated through least-squares fitting of the  $\Delta G_{\text{bind}}$  values calculated for  $\alpha 4\beta 2$  and  $\alpha 7$  nAChRs binding with the protonated structures of the 14 agonists to the available experimental data. The calibrated  $\alpha$ ,  $E_0$ ,  $\beta_{12}$ ,  $\beta_{10}$ , and  $\lambda$  values are 0.521,  $-2.128$ , 5.571, 668.580, and 1.558, respectively, when the energies and distances used are in kcal/mol (for energy) and Å (for distance). The correlation coefficient is 0.90 and the rmsd of the calculated  $\Delta G_{\text{bind}}$  values (for the protonated structures) to the corresponding experimental data is 1.08 kcal/mol.

By use of the calibrated parameters, the calculated  $\Delta G_{\text{HB}}$  and  $\Delta G_{\text{LRE}}$  values are summarized in Table 2, along with the  $\Delta G_{\text{AD}}$  values. Besides the microscopic binding structures and free energies of the protonated structures binding with  $\alpha 4\beta 2$  and  $\alpha 7$  nAChRs, we also examined the microscopic binding structures and free energies of the corresponding deprotonated (neutral) structures binding with  $\alpha 4\beta 2$  and  $\alpha 7$  nAChRs. On the basis of the calibrated parameters discussed above, the calculated  $\Delta G_{\text{HB}}$  and  $\Delta G_{\text{LRE}}$  values are summarized in Table 2, along with the calculated  $\Delta G_{\text{AD}}$  and  $pK_a$  values. By using the calculated



**Table 2.** Energy Results (in kcal/mol) Calculated for Microscopic Binding of  $\alpha 4\beta 2$  and  $\alpha 7$  nAChRs with Protonated and Deprotonated Molecular Species of Agonists

molecular species <sup>a</sup>	pK <sub>a</sub> <sup>b</sup>	binding with $\alpha 4\beta 2$ nAChR			binding with $\alpha 7$ nAChR		
		$\Delta G_{AD}$ <sup>c</sup>	$\Delta G_{HB}$ <sup>d</sup>	$\Delta G_{LRE}$ <sup>e</sup>	$\Delta G_{AD}$ <sup>c</sup>	$\Delta G_{HB}$ <sup>d</sup>	$\Delta G_{LRE}$ <sup>e</sup>
<b>1</b>		-7.41	-1.10	-6.46	-5.96	-1.04	-3.55
deprotonated <b>1</b>	8.9	-6.44	0.00	-0.10	-6.17	0.00	-0.08
<b>2</b>		-9.08	-3.39	-6.06	-7.85	-1.26	-5.16
deprotonated <b>2a</b>	10.8	-7.98	-2.64	-0.02	-7.79	-2.07	0.02
deprotonated <b>2b</b>	10.9	-7.76	0.00	-0.05	-7.65	0.00	-0.08
<b>3</b>		-7.70	-1.19	-5.87	-7.05	-1.11	-3.22
deprotonated <b>3</b>	8.2	-6.25	-0.00	-0.04	-6.01	-0.00	0.00
<b>4</b>		-8.93	-1.37	-6.59	-8.43	-0.81	-2.82
deprotonated <b>4a</b>	7.4	-7.80	-0.13	0.04	-7.53	-0.02	-0.02
deprotonated <b>4b</b>	7.0	-7.81	-0.14	0.08	-7.75	-0.88	0.01
<b>5</b>		-7.41	-4.69	-5.58	-6.67	-3.86	-3.89
deprotonated <b>5a</b>	7.6	-6.51	-0.23	-0.02	-5.89	-0.40	-0.02
deprotonated <b>5b</b>	8.4	-6.43	-0.33	0.02	-5.81	-0.32	0.00
<b>6</b>		-10.94	-1.87	-6.16	-9.76	-0.72	-2.65
deprotonated <b>6a</b>	(10.8)	-9.66	-0.76	-0.03	-8.95	-0.40	-0.04
deprotonated <b>6b</b>	(10.9)	-9.62	-0.62	-0.14	-8.84	0.00	-0.05
<b>7</b>		-7.27	-1.78	-6.36	-7.51	-1.91	-2.63
deprotonated <b>7a</b>	10.2	-6.90	-1.49	0.00	-6.49	-1.44	-0.02
deprotonated <b>7b</b>	6.7	-6.83	-0.78	0.04	-6.43	-0.14	-0.02
<b>8</b>		-9.10	-1.32	-6.03	-8.90	-0.01	-1.70
deprotonated <b>8a</b>	10.6	-7.85	0.00	-0.03	-8.38	-0.01	-0.03
deprotonated <b>8b</b>	10.7	-7.97	-1.72	0.00	-8.33	0.00	-0.05
<b>9</b>		-6.68	-1.13	-4.85	-6.92	-4.60	-4.79
deprotonated <b>9</b>	8.2	-6.84	-0.78	0.08	-6.89	-0.38	0.00
<b>10</b>		-9.26	0.00	-3.79	-10.63	-3.85	-3.83
deprotonated <b>10</b>	(8.2)	-8.95	0.00	0.03	-8.23	-0.84	-0.03
<b>11</b>		-9.29	0.00	-4.97	-10.54	-3.77	-4.11
deprotonated <b>11</b>	(8.2)	-8.92	0.00	-0.07	-8.24	-0.65	0.02
<b>12</b>		-8.43	0.00	-4.64	-10.00	-2.40	-4.36
deprotonated <b>12</b>	(8.2)	-6.53	0.00	0.01	-7.95	-0.13	0.13
<b>13</b>		-8.62	0.00	-4.79	-10.95	-2.48	-4.76
deprotonated <b>13</b>	(8.2)	-7.68	0.00	-0.03	-7.93	-0.10	0.01
<b>14</b>		-8.70	0.00	-4.36	-10.76	-2.11	-4.36
deprotonated <b>14</b>	(8.2)	-7.72	0.00	0.04	-7.65	-0.21	0.06

<sup>a</sup> Each agonist has two or three molecular species, and the first species (as shown in Table 1) is the protonated structure. When the agonist has two protons on the protonated amine (see Table 1), there are two deprotonated structures with slightly different conformations that are designated as “deprotonated” and ending with the letter “a” and “b”. The “a”/“b” refers to the structure in which the deprotonation occurs for the proton on the right/left side based on the protonated structure illustrated in Table 1. <sup>b</sup> pK<sub>a</sub> is estimated for the protonated agonist associated with a given deprotonated structure. The pK<sub>a</sub> values for **6** were considered to be roughly the same as those for **2**. The pK<sub>a</sub> values for **10–14** were all considered to be roughly the same as that for **9** because of their structural similarity. <sup>c</sup>  $\Delta G_{AD}$  represents the binding free energy estimated by using the modified AutoDock 3.0.5 function without contribution from hydrogen bonding. <sup>d</sup>  $\Delta G_{HB}$  is the hydrogen-bonding energy. <sup>e</sup>  $\Delta G_{LRE}$  refers to the long-range electrostatic interaction energy between all ligand atoms and all protein atoms outside the 22.5 Å × 22.5 Å × 22.5 Å box.

microscopic binding free energies and the pK<sub>a</sub> values, we were able to calculate the phenomenological binding free energy for each agonist binding with a receptor at a given pH, according to the “from-microscopic-to-phenomenological binding” approach described in our previous work.<sup>26</sup> The computational determination of the phenomenological binding free energy for a ligand binding with a receptor accounts for the receptor binding with all of the possible molecular species of the ligand. The phenomenological binding free energy is determined by using both the microscopic binding free energies for all of the molecular species and their concentration distribution in solution under a given pH.<sup>26</sup> The phenomenological binding free energies calculated at physiological pH (i.e., pH 7.4) are summarized in Table 3 in comparison with the corresponding experimental data.

As seen in Table 2, the  $\Delta G_{LRE}$  values calculated for the protonated structures binding with a receptor are generally much lower than those calculated for the corresponding deprotonated structures binding with the same receptor. This general trend can be attributed to a common factor for all of these receptor–

**Table 3.** Phenomenological Binding Free Energies ( $\Delta G_{bind}^{all}$ , in kcal/mol) Calculated for Representative Agonists Binding with  $\alpha 4\beta 2$  and  $\alpha 7$  nAChRs in Comparison with Available Experimental Data<sup>a</sup>

agonist	$\Delta G_{bind}^{all}(\alpha 4\beta 2)$		$\Delta G_{bind}^{all}(\alpha 7)$		$\Delta G_{bind}^{all}(\alpha 7) - \Delta G_{bind}^{all}(\alpha 4\beta 2)$	
	calcd	exptl	calcd	exptl	calcd	exptl
<b>1</b>	-10.2 (-10.3)	-12.2	-6.5 (-6.6)	-8.2	3.7 (3.7)	4.0
<b>2</b>	-13.1 (-13.1)	-14.6	-9.4 (-9.4)	-9.5	3.7 (3.7)	5.1
<b>3</b>	-9.9 (-10.0)	-9.9	-6.8 (-6.9)	>-6.8	3.1 (3.1)	>3.1
<b>4</b>	-10.8 (-11.5)	-11.7	-6.2 (-6.9)	-7.9	4.6 (4.6)	3.9
<b>5</b>	-12.7 (-13.0)	-14.8	-9.8 (-10.1)	-10.6	2.9 (2.9)	4.2
<b>6</b>	-12.6 (-12.6)	-13.9	-7.4 (-7.4)	-8.9	5.2 (5.2)	5.0
<b>7</b>	-9.7 (-10.8)	-10.1	-6.2 (-7.3)	>-6.8	3.5 (3.5)	>3.3
<b>8</b>	-11.0 (-11.0)	-10.3	-5.2 (-5.2)	-6.1	5.8 (5.8)	4.2
<b>9</b>	-8.3 (-8.4)	-6.5	-11.8 (-11.9)	-9.6	-3.5 (-3.5)	-3.1
<b>10</b>	-7.3 (-7.4)	>-6.8	-12.0 (-12.1)	-11.6	-4.7 (-4.7)	<-4.8
<b>11</b>	-8.6 (-8.7)	-7.8	-12.2 (-12.3)	-11.0	-3.6 (-3.6)	-3.2
<b>12</b>	-7.8 (-7.9)	>-7.4 <sup>b</sup>	-10.8 (-10.9)	-10.4	-3.0 (-3.0)	<-3.0
<b>13</b>	-8.1 (-8.2)	>-6.8 <sup>b</sup>	-11.7 (-11.8)	-12.0	-3.6 (-3.6)	<-5.2
<b>14</b>	-7.7 (-7.8)	>-7.4 <sup>b</sup>	-10.9 (-11.0)	-11.0	-3.2 (-3.2)	<-3.6

<sup>a</sup> All binding free energies are given in kcal/mol at 298.15 K. The experimental  $\Delta G_{bind}^{all}$  values are derived from the K<sub>d</sub> values listed in Table 1. The values given in parentheses are the microscopic binding free energies calculated for the protonated structures. The microscopic binding free energies are regarded as the phenomenological binding free energies when the deprotonation of the agonists are completely neglected. <sup>b</sup> Estimated from the experimentally measured % inhibition with 1  $\mu$ M **12** or **13** or **14** in the rat brain homogenate binding assays;<sup>25c</sup> thus, 50% inhibition (IC<sub>50</sub>) was extrapolated/estimated from the % inhibition and  $\Delta G_{bind}^{all} = -RT \ln(K_d) \approx -RT \ln(IC_{50})$  because of the lack of the quantitative binding affinity data.

agonist binding structures: the nAChRs are all negatively charged, and negatively charged receptors are generally more attractive to the positively charged structures of the ligands. As mentioned above, the net charges of the LBD are -37e and -20e for  $\alpha 4\beta 2$  and  $\alpha 7$  nAChRs, respectively, but none of the charged amino acid residues interact strongly with any of these agonist structures, according to our docked microscopic binding structures. Relatively, the negatively charged residues of the receptor closer to the ligand contribute more to  $\Delta G_{LRE}$  according to eq 3. Hence, the microscopic binding free energy for an agonist structure binding with an nAChR is the sum of contributions from both the local receptor–ligand binding within the binding pocket and the long-range electrostatic interactions between the positively charged agonist and the negatively charged protein environment outside the binding pocket. The local binding modes of a receptor binding with the protonated and deprotonated structures of an agonist are usually similar except for one hydrogen bond involving the proton that exists only in the protonated ligand structure. Generally speaking, when the energetic contributions from the local binding are close, the contributions from the long-range electrostatic interactions will have a large impact on the different binding of the protonated and deprotonated structures to the receptor. Only when the local binding with the deprotonated structure is significantly stronger than that with the corresponding protonated structure can the microscopic binding free energy calculated for the deprotonated structure be lower than, or close to, that calculated for the corresponding protonated structure. Specifically, for all of the agonists considered in this study, the microscopic binding free energies calculated for the protonated structures are always significantly lower than those calculated for the corresponding deprotonated structures. Thus, the microscopic binding of an agonist binding with  $\alpha 4\beta 2$  and  $\alpha 7$  nAChRs is always dominated by the protonated structure, and therefore, the calculated phenomenological binding free energies are always close to the corresponding microscopic binding free energies calculated for the protonated structures.

In light of the insights obtained from the receptor–ligand electrostatic interactions, one can also understand another general trend regarding the relative binding free energies calculated for the same protonated agonist structure binding to two different nAChR subtypes. As seen in Table 3, the calculated binding free energy of an agonist binding with the  $\alpha 4\beta 2$  nAChR is about 2.9–5.8 kcal/mol lower than that with the  $\alpha 7$  nAChR for all of the  $\alpha 4\beta 2$ -specific agonists in Table 3. This is because, as mentioned above, the microscopic binding modes for a protonated structure binding with  $\alpha 4\beta 2$  and  $\alpha 7$  nAChRs are very similar for all of these agonists. For an agonist with a similar microscopic mode of binding with  $\alpha 4\beta 2$  and  $\alpha 7$  nAChRs, the contributions from the local binding to the microscopic binding free energies of the protonated structure binding with  $\alpha 4\beta 2$  and  $\alpha 7$  nAChRs are close, but the long-range receptor–ligand electrostatic interactions are usually stronger for the binding with the  $\alpha 4\beta 2$  nAChR (whose LBD has a net charge of  $-37e$ ) than for binding with the  $\alpha 7$  nAChR (whose LBD has a net charge of  $-20e$ ), as seen in Table 2. Only when the microscopic binding modes are quite different will the different orientations of the agonist dipole moment significantly affect the difference in the long-range electrostatic interactions.

Each of the  $\alpha 7$ -specific agonists, including **9** and structurally similar compounds, has quite different microscopic modes of binding with  $\alpha 4\beta 2$  and  $\alpha 7$  nAChRs. As seen in Figure 6 and other figures (i.e., Figures S8–S13 of the Supporting Information), the local binding modes of the protonated structures of **9** and related compounds with the  $\alpha 7$  nAChR are much stronger than those of the same agonist structures binding with  $\alpha 4\beta 2$  nAChR. In these special cases, the difference in the local binding mode dominates the difference in the microscopic binding free energy (particularly the calculated  $\Delta G_{\text{HB}}$  value, as seen in Table 2). At the same time, because of the different binding modes, the difference in  $\Delta G_{\text{LRE}}$  is also significantly smaller than those found for the other agonists. This analysis qualitatively explains why the calculated microscopic binding free energy of the protonated **9** structure for binding with the  $\alpha 7$  nAChR is markedly lower than that obtained for its binding with the  $\alpha 4\beta 2$  nAChR by  $\sim 3.5$  kcal/mol.

As seen in Table 3, overall agreement between the calculated and experimental phenomenological binding free energies is good. Subtype selectivity for an agonist binding with  $\alpha 4\beta 2$  and  $\alpha 7$  nAChRs can be represented quantitatively by the difference between the phenomenological binding free energies, i.e.,

$$\Delta\Delta G_{\text{bind}}^{\text{all}} = \Delta G_{\text{bind}}^{\text{all}}(\alpha 7) - \Delta G_{\text{bind}}^{\text{all}}(\alpha 4\beta 2) \quad (4)$$

As seen in Table 3, the calculated  $\Delta\Delta G_{\text{bind}}^{\text{all}}$  values are all in good agreement with the corresponding experimental  $\Delta\Delta G_{\text{bind}}^{\text{all}}$  values, suggesting that the computational protocol developed in this study is suitable not only for reproducing the relative binding free energies of a given nAChR binding with different agonists but also for studying the subtype selectivity of agonists binding with different nAChR subtypes.

**(4) Comparison with Previous Modeling Studies of Subtype Selectivity.** Understanding the subtype selectivity of agonists binding with different nAChR subtypes is critically important for rational drug design targeting specific nAChRs but is very challenging for computational modeling. Very recently, some other molecular docking studies<sup>30d,e</sup> on a series of agonists binding with rat  $\alpha 4\beta 2$  and  $\alpha 3\beta 4$  nAChRs have been reported. Those docking studies were based on the previously reported homology models of  $\alpha 4\beta 2$  (PDB code 1ole) and  $\alpha 3\beta 4$

(PDB code 1olf) nAChRs modeled by other researchers using an earlier X-ray crystal structure of the AChBP as the template. Bisson et al.<sup>30d</sup> docked agonists into the interface cleft of the models by using the FlexX module of the Sybyl software package (Tripos Inc., St. Louis, MO) and then ranked binding affinities by using a consensus scoring (CScore) system (from a minimum of 0 to a maximum of 5). Yuan et al.<sup>30e</sup> performed molecular docking of only five agonists into the postulated binding site of pre-existing models of  $\alpha 4\beta 2$  and  $\alpha 3\beta 4$  nAChRs<sup>30b</sup> even without ranking. The microscopic binding modes obtained from their docking studies are distinctly different from what were obtained in the present study. For example, in our  $\alpha 4\beta 2$  nAChR model, compound **2** does not make contact with  $\beta \text{Lys}77$  at all. According to the microscopic binding structures described by Bisson et al.<sup>30d</sup> and Yuan et al.,<sup>30e</sup> in addition to the cation– $\pi$  interactions with the  $\alpha 4\beta 2$  nAChR, the pyridine nitrogen atoms of epibatidine and **2** also exhibit hydrogen bonding with the positively charged side chain of  $\beta \text{Lys}77$  of the  $\beta 2$  subunit, and the pyridine ring makes contacts with the aromatic side chains of  $\alpha \text{Tyr}188$  and  $\alpha \text{Tyr}195$  of the  $\alpha 4$  subunit at the bottom of the aromatic cage.<sup>30d,e</sup> The additional hydrogen bonding with  $\beta \text{Lys}77$  was considered in the studies by Bisson et al.<sup>30d</sup> and Yuan et al.<sup>30e</sup> as a major structural factor for the exceptionally high binding affinity of epibatidine and **2** with the  $\alpha 4\beta 2$  nAChR. In addition, the binding of epibatidine and **2** with the  $\alpha 3\beta 4$  nAChR was considered to be weakened by an Ile residue of the  $\beta 4$  subunit at a reciprocal position as  $\beta \text{Lys}77$  in the  $\beta 2$  subunit.<sup>30d,e</sup> The role of  $\beta \text{Lys}77$  was replaced by the neutral side chain of  $\beta \text{Gln}115$  of the  $\beta 4$  subunit, which forms hydrogen bonds with the same pyridine nitrogen atom of epibatidine and **2**. Bisson et al.<sup>30d</sup> and Yuan et al.<sup>30e</sup> attributed these differences to structural determinants for the much lower binding affinities of epibatidine and **2** with the  $\alpha 4\beta 2$  nAChR.

The remarkable discrepancy between our modeled microscopic binding structures and those reported by Bisson et al.<sup>30d</sup> and Yuan et al.<sup>30e</sup> may be attributed to the fact that the nAChR models used in the docking studies were built using different templates. The nAChR models used by Bisson et al.<sup>30d</sup> and Yuan et al.<sup>30e</sup> were built by other researchers<sup>30a–c</sup> using an earlier X-ray crystal structure of the AChBP. The construction of those nAChR models did not consider the conformational rearrangements during agonist binding;<sup>30a,b</sup> the models were regarded as lacking the rearrangements of the protein, and “thus these models are not very good” in comparison with the subsequently reported X-ray crystal structure of nicotine-bound AChBP.<sup>27b</sup> Our nAChR models were constructed on the basis of the newer X-ray crystal structure of the nicotine-bound AChBP.<sup>27b</sup> After the initial structural models were built, a series of geometric optimizations were performed on both the pure nAChR models and each of their agonist-bound structures to further refine the modeled structures. It is emphasized that our  $\alpha 4\beta 2$  nAChR model and its binding with **2** were constructed and published<sup>26</sup> prior to publication of the latest X-ray crystal structure of the AChBP–epibatidine complex,<sup>31a</sup> although our own  $\alpha 7$  nAChR model is reported for the first time in the present study. It is generally believed that the agonist binding with an nAChR should be very similar to the corresponding binding with AChBP. Our modeled microscopic binding mode between the  $\alpha 4\beta 2$  nAChR and **2** is consistent with that in the subsequently reported X-ray crystal structure of the AChBP–epibatidine complex.<sup>31a</sup> This agreement suggests that our modeled nAChR models and their microscopic binding modes with the agonist molecules are more reasonable.

In addition, we have demonstrated, in the present study for the first time, that the subtype selectivity for an agonist binding with two different nAChR subtypes is dominated by the long-range receptor–agonist electrostatic interactions.

## Conclusion

The present computational modeling study indicates that the agonist binding pocket of the  $\alpha 7$  nAChR is very similar to that of the  $\alpha 4\beta 2$  nAChR. A major structural difference between  $\alpha 7$  and  $\alpha 4\beta 2$  nAChRs exists in the complementary side of the receptor; i.e., there is a hydrophilic amino acid residue Gln116 of the  $\alpha 7$  nAChR that corresponds to an aromatic residue  $\beta$ Phe117 of the  $\alpha 4\beta 2$  nAChR.

All of the computational results demonstrate that the subtype-selective binding of agonists with  $\alpha 4\beta 2$  and  $\alpha 7$  nAChRs is affected not only by local binding but also by long-range electrostatic interactions between the receptors and the protonated structures of the agonists. The effects of the long-range electrostatic interactions on receptor subtype selectivity are primarily due to the distinct difference in the net charge of the LBD between the two nAChR subtypes ( $-37e$  for  $\alpha 4\beta 2$  and  $-20e$  for  $\alpha 7$ ). For  $\alpha 4\beta 2$ -selective agonists, the microscopic binding modes for the  $\alpha 4\beta 2$  nAChR are very similar to the corresponding binding modes for the  $\alpha 7$  nAChR, and therefore, the subtype selectivity of these agonists binding to  $\alpha 4\beta 2$  and  $\alpha 7$  nAChRs is dominated by the long-range electrostatic interactions. Especially, for **9** and related compounds, their microscopic binding modes with the  $\alpha 7$  nAChR are remarkably different from those with the  $\alpha 4\beta 2$  nAChR so that the local binding (including the hydrogen bonding and cation– $\pi$  interaction) with the  $\alpha 7$  nAChR is much stronger than that with the  $\alpha 4\beta 2$  nAChR. For example, the present study suggests that nAChR agonists can apparently gain selectivity for the  $\alpha 7$  nAChR if they have an H-bond donor and are able to form a tight water-mediated H-bond network with Q116.

On the basis of the determined microscopic binding and  $pK_a$  and the computational protocol developed in this study, the calculated phenomenological binding free energies are in good agreement with the available experimental data for both the relative binding free energies with regard to the subtype selectivity of agonists binding to the two different nAChR subtypes. The fundamental insights obtained in the present computational study are expected to be valuable for future rational design of the subtype-selective agonists targeted to specific nAChR subtypes.

**Acknowledgment.** This research was supported in part by Kentucky Science & Engineering Foundation Grant KSEF-925-RDE-008, by the Center for Computational Sciences (CCS) at University of Kentucky, and by NIH Grant U19DA017548. We also utilized the EMSL Molecular Sciences Computing Facility (a DOE National User facility operated by Pacific Northwest National Laboratory) under Grand Challenge Grants GC3565 and GC9598. Dr. Xi Chen thanks his home institute (Central China Normal University) for allowing him to work at University of Kentucky as a postdoctoral researcher.

**Supporting Information Available:** An additional figure for key internuclear distances obtained from MD simulations and 13 stereoviews of the microscopic binding of  $\alpha 4\beta 2$  and  $\alpha 7$  nAChRs with the examined protonated agonists. This material is available free of charge via the Internet at <http://pubs.acs.org>.

## References

- (1) Dougherty, D. A.; Lester, H. A. Snails, synapses and smokers. *Nature* **2001**, *411*, 252–255.
- (2) Unwin, N.; Miyazawa, A.; Li, J.; Fujiyoshi, Y. Activation of the nicotinic acetylcholine receptor involves a switch in conformation of the  $\alpha$  subunits. *J. Mol. Biol.* **2002**, *319*, 1165–1176.
- (3) Shen, X.-M.; Ohno, K.; Tsujino, A.; Brengman, J. M.; Gingold, M.; Sine, S. M.; Engel, A. G. Mutation causing severe myasthenia reveals functional asymmetry of AChR signature cystine loops in agonist binding and gating. *J. Clin. Invest.* **2003**, *111*, 497–505.
- (4) Miyazawa, A.; Fujiyoshi, Y.; Unwin, N. Structure and gating mechanism of the acetylcholine receptor core. *Nature* **2003**, *423*, 949–955.
- (5) Li, S.-P.; Park, M. S.; Kim, J. H.; Kim, M. O. Chronic nicotine and smoke treatment modulate dopaminergic activities in ventral tegmental area and nucleus accumbens and the  $\gamma$ -aminobutyric acid type B receptor expression of the rat prefrontal cortex. *J. Neurosci. Res.* **2004**, *78*, 868–879.
- (6) Matsubayashia, M.; Inoueb, A.; Amanoa, T.; Sekia, T.; Nakatab, Y.; Sasac, M.; Sakai, N. Involvement of  $\alpha 7$  and  $\alpha 4\beta 2$ -type postsynaptic nicotinic acetylcholine receptors in nicotine-induced excitation of dopaminergic neurons in the substantia nigra: a patch clamp and single-cell PCR study using acutely dissociated nigral neurons. *Mol. Brain Res.* **2004**, *129*, 1–7.
- (7) Quik, M. Smoking, nicotine and Parkinson's disease. *Trends Neurosci.* **2004**, *27*, 561–568.
- (8) Lester, H. A.; Dibas, M. I.; Dahan, D. S.; Leite, J. F.; Dougherty, D. A. Cys-loop receptors: new twists and turns. *Trends Neurosci.* **2004**, *27*, 329–336.
- (9) Jensen, A. A.; Frolund, B.; Liljefors, T.; Krogsgaard-Larsen, P. Neuronal nicotinic acetylcholine receptors: structural revelations, target identifications, and therapeutic inspirations. *J. Med. Chem.* **2005**, *48*, 4705–4745.
- (10) Cashin, A. L.; Petersson, E. J.; Lester, H. A.; Dougherty, D. A. Using physical chemistry to differentiate nicotinic from cholinergic agonists at the nicotinic acetylcholine receptor. *J. Am. Chem. Soc.* **2005**, *127*, 350–356.
- (11) Hernandez, C. M.; Terry, A. V., Jr. Repeated nicotine exposure in rats: effects on memory function, cholinergic markers and nerve growth factor. *Neuroscience* **2005**, *130*, 997–1012.
- (12) Cao, Y.-J.; Surowy, C. S.; Puttfarcken, P. S. Different nicotinic acetylcholine receptor subtypes mediating striatal and prefrontal cortical [ $^3$ H]dopamine release. *Neuropharmacology* **2005**, *48*, 72–79.
- (13) (a) Hogg, R. C.; Bertrand, D. What genes tell us about nicotine addiction. *Science* **2004**, *306*, 983–985. (b) Tapper, A. R.; McKinney, S. L.; Nashmi, R.; Schwarz, J.; Deshpande, P.; Labarca, C.; Whiteaker, P.; Marks, M. J.; Collins, A. C.; Lester, H. A. Nicotine activation of  $\alpha 4^*$  receptors: sufficient for reward, tolerance, and sensitization. *Science* **2004**, *306*, 1029–1032. (c) King, S. L.; Caldarone, B. J.; Picciotto, M. R.  $\beta 2$ -subunit-containing nicotinic acetylcholine receptors are critical for dopamine-dependent locomotor activation following repeated nicotine administration. *Neuropharmacology* **2004**, *47*, 132–139. (d) Bao, J.; Lei, D.; Du, Y.; Ohlemiller, K. K.; Beaudet, A. L.; Role, L. W. Requirement of nicotinic acetylcholine receptor subunit  $\beta 2$  in the maintenance of spiral ganglion neurons during aging. *J. Neurosci.* **2005**, *25*, 3041–3045. (e) Fischer, H.; Liu, D.-M.; Lee, A.; Harries, J. C.; Adams, D. J. Selective modulation of neuronal nicotinic acetylcholine receptor channel subunits by Go-protein subunits. *J. Neurosci.* **2005**, *25*, 3571–3577. (f) Person, A. M.; Bills, K. L.; Liu, H.; Botting, S. K.; Lindstrom, J.; Wells, G. B. Extracellular domain nicotine acetylcholine receptors formed by  $\alpha 4$  and  $\beta 2$  subunits. *J. Biol. Chem.* **2005**, *280*, 39990–40002.
- (14) (a) Lyford, L. K.; Sproul, A. D.; Eddins, D.; McLaughlin, J. T.; Rosenberg, R. L. Agonist-induced conformational changes in the extracellular domain of  $\alpha 7$  nicotinic acetylcholine receptors. *Mol. Pharmacol.* **2003**, *64*, 650–658. (b) Grassi, F.; Palma, E.; Tonini, R.; Amici, M.; Ballivet, M.; Eusebi, F. Amyloid  $\beta_{1-42}$  peptide alters the gating of human and mouse  $\alpha$ -bungarotoxin-sensitive nicotinic receptors. *J. Physiol.* **2003**, *547*, 147–157. (c) Buckingham, S. D.; Pym, L.; Jones, A. K.; Brown, L.; Sansom, M. S. P.; Sattelle, D. B.; Biggin, P. C. A7DB: a relational database for mutational, physiological and pharmacological data related to the  $\alpha 7$  nicotinic acetylcholine receptor. *BMC Neurosci.* **2005**, *6*, 1–4. (d) De Rosa, M. J.; Esandi, M. D.; Garelli, A.; Rayes, D.; Bouzat, C. Relationship between  $\alpha 7$  nAChR and apoptosis in human lymphocytes. *J. Neuroimmunol.* **2005**, *160*, 154–161. (e) Criado, M.; Mulet, J.; Bernal, J. A.; Gerber, S.; Sala, S.; Sala, F. Mutations of a conserved lysine residue in the N-terminal domain of  $\alpha 7$  nicotine receptors affect gating and binding of nicotine agonists. *Mol. Pharmacol.* **2005**, *68*, 1669–1677. (f) de Fiebre, N. E.; de Fiebre, C. M.  $\alpha 7$  nicotinic acetylcholine receptor knockout selectively enhances ethanol-, but not  $\beta$ -amyloid-induced neurotoxicity. *Neurosci. Lett.* **2005**, *373*, 42–47.

- (15) (a) Schmitt, J. D. Exploring the nature of molecular recognition in nicotinic acetylcholine receptors. *Curr. Med. Chem.* **2000**, *7*, 749–800. (b) Tonder, J. E.; Olesen, P. H. Agonists at the  $\alpha 4\beta 2$  nicotinic acetylcholine receptors: structure–activity relationships and molecular modeling. *Curr. Med. Chem.* **2001**, *8*, 651–674. (c) Bunnelle, W. H.; Dart, M. J.; Schrimpf, M. R. Design of ligands for the nicotinic acetylcholine receptors: the quest for selectivity. *Curr. Top. Med. Chem.* **2004**, *4*, 299–334. (d) Briggs, C. A.; Anderson, D. J.; Brioni, J. D.; Buccafusco, J. J.; Buckley, M. J.; Campbell, J. E.; Decker, M. W.; Donnelly-Roberts, D.; Elliott, R. L.; Gopalakrishnan, M.; Holladay, M. W.; Hui, Y. H.; Jackson, W. J.; Kim, D. J.; Marsh, K. C.; O'Neill, A.; Prendergast, M. A.; Ryther, K. B.; Sullivan, J. P.; Arneric, S. P. Functional characterization of the novel neuronal nicotinic acetylcholine receptor ligand GTS-21 in vitro and in vivo. *Pharmacol. Biochem. Behav.* **1997**, *57*, 231–241.
- (16) (a) Dwoskin, L. P.; Sumithran, S. P.; Zhu, J.; Deaciuc, A. G.; Ayers, J. T.; Crooks, P. A. Subtype-selective nAChR antagonists: potential as tobacco use cessation agents. *Bioorg. Med. Chem. Lett.* **2004**, *14*, 1863–1867. (b) Crooks, P. A.; Ayers, J. T.; Xu, R.; Sumithran, S. P.; Grinevich, V. P.; Wilkins, L. H.; Deaciuc, A. G.; Allen, D. D.; Dwoskin, L. P. Development of subtype-selective ligands as antagonists at nAChRs mediating nicotine-evoked dopamine release. *Bioorg. Med. Chem. Lett.* **2004**, *14*, 1869–1874. (c) Papke, R. L.; Zheng, G.; Horenstein, N. A.; Dwoskin, L. P.; Crooks, P. A. The characterization of a novel rigid nicotine analog with  $\alpha 7$ -selective nAChR agonist activity and modulation of agonist properties by boron inclusion. *Bioorg. Med. Chem. Lett.* **2005**, *15*, 3874–3880.
- (17) (a) Carroll, F. I.; Liang, F.; Navarro, H. A.; Brieady, L. E.; Abraham, P.; Damaj, M. I.; Martin, B. R. Synthesis, nicotinic acetylcholine receptor binding, and antinociceptive properties of 2-exo-2-(2'-substituted 5'-pyridinyl)-7-azabicyclo[2.2.1]heptanes. Epibatidine analogues. *J. Med. Chem.* **2001**, *44*, 2229–2237. (b) Cox, C. D.; Malpass, J. R.; Gordon, J.; Rosen, R. Synthesis of epibatidine isomers: endo-5- and 6-(6'-chloro-3'-pyridyl-2-azabicyclo[2.2.1]-heptanes. *J. Chem. Soc., Perkin Trans. 1* **2001**, 2372–2379. (c) Carrol, F. I. Epibatidine structure–activity relationships. *Bioorg. Med. Chem. Lett.* **2004**, *14*, 1889–1896. (d) White, R.; Malpass, J. R.; Handa, S.; Baker, S. R.; Broad, L. M.; Folly, L.; Mogg, A. Epibatidine isomers and analogues: structure–activity relationships. *Bioorg. Med. Chem. Lett.*, in press.
- (18) (a) Arneric, S. P.; Sullivan, J. P.; Briggs, C. A.; Donnelly-Roberts, D.; Anderson, D. J.; Raszkievicz, J. L.; Hughes, M. L.; Cadman, E. D.; Adams, P.; Garvey, D. S. (S)-3-Methyl-5-(1-methyl-2-pyrrolidinyl) isoxazole (ABT 418): a novel cholinergic ligand with cognition-enhancing and anxiolytic activities: I. In vitro characterization. *J. Pharmacol. Exp. Ther.* **1994**, *270*, 310–318. (b) Avenzo, A.; Busto, J. H.; Cativiela, C.; Dordal, A.; Frigola, J.; Peregrina, J. M. Synthesis, activity and theoretical study of ABT-418 analogues. *Tetrahedron* **2002**, *58*, 4505–4511.
- (19) Sharples, C. G. V.; Karig, G.; Simpson, G. L.; Spencer, J. A.; Wright, E.; Millar, N. S.; Wonnacott, S.; Gallagher, T. Synthesis and pharmacological characterization of novel analogues of the nicotinic acetylcholine receptor agonist ( $\pm$ )-UB-165. *J. Med. Chem.* **2002**, *45*, 3235–3245.
- (20) (a) Sullivan, J. P.; Donnelly-Roberts, D.; Briggs, C. A.; Anderson, D. J.; Gopalakrishnan, M.; Piattoni-Kaplan, M.; Campbell, J. E.; Mckenna, D. G.; Molinari, E.; Hettinger, A.-M.; Garvey, D. S.; Wasicak, J. T.; Holladay, M. W.; Williams, M.; Arneric, S. P. A-85380 [3-(2(s)-azetidylmethoxy) pyridine]: in vitro pharmacological properties of a novel, high affinity  $\alpha 4\beta 2$  nicotinic acetylcholine receptor ligand. *Neuropharmacology* **1996**, *35*, 725–734. (b) Gallezot, J.-D.; Bottlaender, M.; Gregoire, M. C.; Roumenov, D.; Deverre, J.-R.; Coulon, C.; Ottaviani, M.; Dolle, F.; Syrota, A.; Valette, H. In vivo imaging of human cerebral nicotinic acetylcholine receptors with 2-<sup>18</sup>F-fluoro-A-85380 and PET. *J. Nucl. Med.* **2005**, *46*, 240–247.
- (21) Coe, J. W.; Brooks, P. R.; Vetelino, M. G.; Wirtz, M. C.; Arnold, E. P.; Huang, J.; Sands, S. B.; Davis, T. I.; Lebel, L. A.; Fox, C. B.; Shrikhande, A.; Heym, J. H.; Schaeffer, E.; Rollema, H.; Lu, Y.; Mansbach, R. S.; Chambers, L. K.; Rovetti, C. C.; Schulz, D. W.; Tingley, F. D., III; O'Neill, B. T. Varenicline: an  $\alpha 4\beta 2$  nicotine receptor partial agonist for smoking cessation. *J. Med. Chem.* **2005**, *48*, 3474–3477.
- (22) (a) Sullivan, J. P.; Donnelly-Roberts, D.; Briggs, C. A.; Anderson, D. J.; Gopalakrishnan, M.; Xue, I. C.; Piattoni-Kaplan, M.; Molinari, E.; Campbell, J. E.; Mckenna, D. G.; Gunn, D. E.; Lin, N.-H.; Ryther, K. B.; He, Y.; Holladay, M. W.; Wonnacott, S.; Williams, M.; Arneric, S. P. ABT-089 [2-methyl-3-(2-(S)-pyrrolidinylmethoxy) pyridine]: I. a potent and selective cholinergic channel modulator with neuroprotective properties. *J. Pharmacol. Exp. Ther.* **1997**, *283*, 235–246. (b) Efange, S. M. N.; Tu, Z.; Hohenberg, K.; Francesconi, L.; Howell, R. C.; Rampersad, M. V.; Todaro, L. J.; Papke, R. L.; Kung, M.-P. 2-(2-Piperidyl)- and 2-(2-pyrrolidyl) chromans as nicotine agonists: synthesis and preliminary pharmacological characterization. *J. Med. Chem.* **2001**, *44*, 4704–4715.
- (23) (a) Ben cherif, M.; Lovette, M. E.; Fowler, K. W.; Arrington, S.; Reeves, L.; Caldwell, W. S.; Lippiello, P. M. RJR-2403: a nicotinic agonist with CNS selectivity. I. In vitro characterization. *J. Pharmacol. Exp. Ther.* **1996**, *279*, 1413–1421. (b) Papke, R. L.; Webster, J. C.; Lippiello, P. M.; Bencherif, M.; Francis, M. M. The activation and inhibition of human nicotinic acetylcholine receptor by RJR-2403 indicate a selectivity for the  $\alpha 4\beta 2$  receptor subtype. *J. Neurochem.* **2000**, *75*, 204–216.
- (24) (a) Mullen, G.; Napier, J.; Balestra, M.; DeCory, T.; Hale, G.; Macor, J.; Mack, R.; Loch, J., III; Wu, E.; Kover, A.; Verhoest, P.; Sampognaro, A.; Phillips, E.; Zhu, Y.; Murray, R.; Griffith, R.; Blosser, J.; Curley, D.; Machulskis, A.; Zongrone, J.; Rosen, A.; Gordon, J. (-)-Spiro[1-azabicyclo[2.2.2]octane-3,5'-oxazolidin-2'-one], a conformationally restricted analogue of acetylcholine, is a highly selective full agonist at the  $\alpha 7$  nicotinic acetylcholine receptor. *J. Med. Chem.* **2000**, *43*, 4045–4050. (b) Kampen, M.; Selbach, K.; Schneider, R.; Schiegel, E.; Boess, F.; Schreiber, R. AR-R 17779 improves social recognition in rats by activation of nicotinic  $\alpha 7$  receptors. *Psychopharmacology* **2004**, *172*, 375–383. (c) Bodnar, A. L.; Cortes-Burgos, L. A.; Cook, K. K.; Dinh, D. M.; Groppi, V. E.; Hajos, M.; Higdon, N. R.; Hoffmann, W. E.; Hurst, R. S.; Myers, J. K.; Rogers, B. N.; Wall, T. M.; Wolfe, M. L.; Wong, E. Discovery and structure–activity relationship of quinuclidine benzamides as agonists of  $\alpha 7$  nicotinic acetylcholine receptors. *J. Med. Chem.* **2005**, *48*, 905–908.
- (25) (a) Tatsumi, R.; Fujio, M.; Takahashi, S.; Numata, A.; Katayama, J.; Satoh, H.; Shiigi, Y.; Maeda, J.; Kuriyama, M.; Horikawa, T.; Murozono, T.; Hashimoto, K.; Tanaka, H. (R)-3'-(3-Methylbenzo[b]thiophen-5-yl)spiro[1-azabicyclo[2.2.2]octane-3,5'-oxazolidin]-2'-one, a novel and potent  $\alpha 7$  nicotinic acetylcholine receptor partial agonist displays cognitive enhancing properties. *J. Med. Chem.* **2006**, *49*, 4374–4383. (b) Tatsumi, R.; Fujio, M.; Satoh, H.; Katayama, J.; Takahashi, S.-I.; Hashimoto, K.; Tanaka, H. Discovery of the  $\alpha 7$  nicotine acetylcholine receptor agonists. (R)-3'-(5-Chlorothiophen-2-yl)spiro-1-azabicyclo[2.2.2]octane-3,5'-[1',3']-oxazolidin-2'-one as a novel, potent, selective, and orally bioavailable ligand. *J. Med. Chem.* **2005**, *48*, 2678–2686. (c) Hajós, M.; Hurst, R. S.; Hoffmann, W. E.; Krause, M.; Wall, T. M.; Higdon, N. R.; Groppi, V. E. The selective  $\alpha 7$  nicotinic acetylcholine receptor agonist PNU-282987 [N-[(3R)-1-azabicyclo[2.2.2]oct-3-yl]-4-chlorobenzamide hydrochloride] enhances GABAergic synaptic activity in brain slices and restores auditory gating deficits in anesthetized rats. *J. Pharmacol. Exp. Ther.* **2005**, *312*, 1213–1222. (d) Wishka, D. G.; Walker, D. P.; Yates, K. M.; Reitz, S. C.; Jia, S.; Myers, K.; Olson, K. L.; Jacobsen, E. J.; Wolfe, M. L.; Groppi, V. E.; Hanchar, A. J.; Thornburgh, B. A.; Cortes-Burgos, L. A.; Wong, E. H.; Staton, B. A.; Raub, T. J.; Higdon, N. R.; Wall, T. M.; Hurst, R. S.; Walters, R. R.; Hoffmann, W. E.; Hajos, M.; Franklin, S.; Carey, G.; Gold, L. H.; Cook, K. K.; Sands, S. B.; Zhao, S. X.; Soglia, J. R.; Kalgutkar, A. S.; Arneric, S. P.; Rogers, B. N. Discovery of N-[(3R)-1-azabicyclo[2.2.2]oct-3-yl]furo[2,3-c]pyridine-5-carboxamide, an agonist of the  $\alpha 7$  nicotinic acetylcholine receptor, for the potential treatment of cognitive deficits in schizophrenia: synthesis and structure–activity relationship. *J. Med. Chem.* **2006**, *49*, 4425–4436.
- (26) Huang, X.; Zheng, F.; Crooks, P. A.; Dwoskin, L.; Zhan, C.-G. Multiple structures of nicotine, (-)-deschloroepibatidine interacting with  $\alpha 4\beta 2$  nicotinic acetylcholine receptor: from microscopic binding to phenomenological binding affinity. *J. Am. Chem. Soc.* **2005**, *127*, 14401–14414.
- (27) (a) Brejc, K.; Dijk, W. J.; Klaassen, R. V.; Schuurmans, M.; Oost, J.; Smit, A. B.; Sixma, T. K. Crystal structure of an ACh-binding protein reveals the ligand-binding domain of nAChRs. *Nature* **2001**, *411*, 269–276. (b) Celie, P. H. N.; Rossum-Fikkert, S. E.; Dijk, W. J.; Brejc, K.; Smit, A. B.; Sixma, T. K. Nicotine and carbamylcholine binding to nicotinic acetylcholine receptors as studied in AChBP crystal structures. *Neuron* **2004**, *41*, 907–914.
- (28) Unwin, N. Refined structure of the nicotinic acetylcholine receptor at 4 Å resolution. *J. Mol. Biol.* **2005**, *346*, 967–989.
- (29) Hansen, S. B.; Radic, Z.; Talley, T. T.; Molles, B. E.; Deerinck, T.; Tsigelny, I.; Taylor, P. Tryptophan fluorescence reveals conformational changes in the acetylcholine binding protein. *J. Biol. Chem.* **2002**, *277*, 41299–41302.
- (30) (a) Schapira, M.; Abagyan, R.; Totrov, M. Structural model of nicotinic acetylcholine receptor isotypes bound to acetylcholine and nicotine. *BMC Struct. Biol.* **2002**, *2*, 1–8. (b) Le Novere, N.; Grutter, T.; Changeux, J. Models of the extracellular domain of the nAChRs and of agonist- and Ca<sup>2+</sup>-binding sites. *Proc. Natl. Acad. Sci. U.S.A.* **2002**, *99*, 3210–3215. (c) Fruchart-Gaillard, C.; Gilquin, B.; Antil-Delbeke, S.; Le Novere, N.; Tamiya, T.; Corringier, P.-J.; Changeux,

- J.-P.; Menez, A.; Servent, D. Experimentally based model of a complex between a snake toxin and the  $\alpha 7$  nicotinic receptor. *Proc. Natl. Acad. Sci. U.S.A.* **2002**, *99*, 3216–3221. (d) Bisson, H. W.; Scapozza, L.; Westera, G.; Mu, L.; Schubiger, P. A. Ligand selectivity for the acetylcholine binding site of the rat  $\alpha 4\beta 2$  and  $\alpha 3\beta 4$  nicotinic subtypes investigated by molecular docking. *J. Med. Chem.* **2005**, *48*, 5123–5130. (e) Yuan, H.; Petukhov, P. A. Computational evidence for the ligand selectivity to the  $\alpha 4\beta 2$  and  $\alpha 3\beta 4$  nicotinic acetylcholine receptors. *Bioorg. Med. Chem.*, in press.
- (31) (a) Hansen, S. B.; Sulzenbacher, G.; Huxford, T.; Marchot, P.; Taylor, P.; Bourne, Y. Structure of alypsia AChBP complexes with nicotine agonists and antagonists revealed distinctive binding interfaces and conformations. *EMBO J.* **2005**, *24*, 3635–3646. (b) Bourne, Y.; Talley, T. T.; Hansen, S. B.; Taylor, P.; Marchot, P. Crystal structure of a CbtX-AChBP complex reveals essential interactions between snake a-neurotoxins and nicotine receptors. *EMBO J.* **2005**, *24*, 1512–1522.
- (32) Thompson, J. D.; Higgins, D. G.; Gibson, T. J. CLUSTAL W: improving the sensitivity of progressive multiple sequence alignment through sequence weighting, position-specific gap penalties, and weight matrix choice. *Nucleic Acids Res.* **1994**, *22*, 4673–4680.
- (33) Henikoff, S.; Henikoff, J. G. Amino-acid substitution matrices from protein blocks. *Proc. Natl. Acad. Sci. U.S.A.* **1992**, *89*, 10915–10919.
- (34) Case, D. A.; Pearlman, D. A.; Caldwell, J. W.; Cheatham, T. E., III; Wang, J.; Ross, W. S.; Simmerling, C. L.; Darden, T. A.; Merz, K. M.; Stanton, R. V.; Cheng, A. L.; Vincent, J. J.; Crowley, M.; Tsui, V.; Gohlke, H.; Radmer, R. J.; Duan, Y.; Pitera, J.; Massova, I.; Seibel, G. L.; Singh, U. C.; Weiner, P. K.; Kollman, P. A. AMBER 7, University of California, San Francisco, 2002.
- (35) (a) Laskowski, R. A.; MacArthur, M. W.; Moss, D. S.; Thornton, J. M. PROCHECK: a program to check the stereochemical quality of protein structures. *J. Appl. Crystallogr.* **1993**, *26*, 283–291. (b) Vriend, G. WHAT IF: A molecular modeling and drug design program. *J. Mol. Graphics* **1990**, *8*, 52–56.
- (36) Jorgensen, W. L.; Chandrasekhar, J.; Madura, J. D.; Impey, R. W.; Klein, M. L. Comparison of Simple Potential Functions for Simulating Liquid Water. *J. Chem. Phys.* **1983**, *79*, 926–935.
- (37) (a) Zhan, C.-G.; Norberto de Souza, O.; Rittenhouse, R.; Ornstein, R. L. Determination of two structural forms of catalytic bridging ligand in zinc-phosphotriesterase by molecular dynamics simulation and quantum chemical calculation. *J. Am. Chem. Soc.* **1999**, *121*, 7279–7282. (b) Koca, J.; Zhan, C.-G.; Rittenhouse, R.; Ornstein, R. L. Mobility of the active site bound paraoxon and sarin in zinc-phosphotriesterase by molecular dynamics simulation and quantum chemical calculation. *J. Am. Chem. Soc.* **2001**, *123*, 817–826. (c) Koca, J.; Zhan, C.-G.; Rittenhouse, R. C.; Ornstein, R. L. Coordination number of zinc ions in phosphotriesterase active site by molecular dynamics and quantum mechanics. *J. Comput. Chem.* **2003**, *24*, 368–378. (d) Zhan, C.-G.; Zheng, F.; Landry, D. W. Fundamental reaction mechanism for cocaine metabolism in human butyrylcholinesterase. *J. Am. Chem. Soc.* **2003**, *125*, 2462–2474. (e) Hamza, A.; Cho, H.; Tai, H.-H.; Zhan, C.-G. Molecular dynamics simulation of cocaine binding with human butyrylcholinesterase and its mutants. *J. Phys. Chem. B* **2005**, *109*, 4776–4782. (f) Hamza, A.; Cho, H.; Tai, H.-H.; Zhan, C.-G. Understanding human 15-hydroxyprostaglandin dehydrogenase binding with NAD<sup>+</sup> and PGE<sub>2</sub> by homology modeling, docking and molecular dynamics simulation. *Bioorg. Med. Chem.* **2005**, *13*, 4544–4551. (g) Pan, Y.; Gao, D.; Yang, W.; Cho, H.; Yang, G.-F.; Tai, H.-H.; Zhan, C.-G. Computational redesign of human butyrylcholinesterase for anti-cocaine medication. *Proc. Natl. Acad. Sci. U.S.A.* **2005**, *102*, 16656–16661. (h) Gao, D.; Zhan, C.-G. Modeling effects of oxyanion hole on the ester hydrolyses catalyzed by human cholinesterases. *J. Phys. Chem. B* **2005**, *109*, 23070–23076. (i) Gao, D.; Zhan, C.-G. Modeling evolution of hydrogen bonding and stabilization of transition states in the process of cocaine hydrolysis catalyzed by human butyrylcholinesterase. *Proteins* **2006**, *62*, 99–110. (j) Hamza, A.; Zhan, C.-G. How can (–)-epigallocatechin gallate from green tea prevent HIV-1 virus infection? Mechanistic insights from computational modeling and the implication for rational design of anti-HIV-1 entry inhibitors. *J. Phys. Chem. B* **2006**, *110*, 2910–2917.
- (38) Berendsen, H. J. C.; Postma, J. P. M.; van Gunsteren, W. F.; DiNola, A.; Haak, J. R. Molecular dynamics with coupling to an external bath. *J. Chem. Phys.* **1984**, *81*, 3684–3690.
- (39) (a) Darden, T.; York, D.; Pedersen, L. Particle mesh Ewald—an Nlog(N) method for Ewald sums in large systems. *J. Chem. Phys.* **1993**, *98*, 10089–10092. (b) Essmann, U.; Perera, L.; Berkowitz, M. L.; Darden, T.; Lee, H.; Pedersen, L. G. A smooth particle mesh Ewald method. *J. Chem. Phys.* **1995**, *103*, 8577–8593.
- (40) Ryckaert, J. P.; Cicotti, G.; Berendsen, H. J. C. Numerical integration of the Cartesian equations of motion of a system with constraints: Molecular dynamics of n-alkanes. *J. Comput. Phys.* **1977**, *23*, 327–341.
- (41) (a) Becke, A. D. Density-functional thermochemistry 3: the role of exact exchange. *J. Chem. Phys.* **1993**, *98*, 5648–5652. (b) Lee, C.; Yang, W.; Parr, R. G. Development of the Colle–Salvetti correlation-energy formula into a functional of the electron-density. *Phys. Rev. B* **1988**, *37*, 785–789. (c) Stephens, P. J.; Devlin, F. J.; Chabalowski, C. F.; Frisch, M. J. *Ab initio* calculation of vibrational absorption and circular-dichroism spectra using density-functional force-fields. *J. Phys. Chem.* **1994**, *98*, 11623–11627.
- (42) Frisch, M. J.; Trucks, G. W.; Schlegel, H. B.; Scuseria, G. E.; Robb, M. A.; Cheeseman, J. R.; Montgomery, J. A., Jr.; Vreven, T.; Kudin, K. N.; Burant, J. C.; Millam, J. M.; Iyengar, S. S.; Tomasi, J.; Barone, V.; Mennucci, B.; Cossi, M.; Scalmani, G.; Rega, N.; Petersson, G. A.; Nakatsuji, H.; Hada, M.; Ehara, M.; Toyota, K.; Fukuda, R.; Hasegawa, J.; Ishida, M.; Nakajima, T.; Honda, Y.; Kitao, O.; Nakai, H.; Klene, M.; Li, X.; Knox, J. E.; Hratchian, H. P.; Cross, J. B.; Adamo, C.; Jaramillo, J.; Gomperts, R.; Stratmann, R. E.; Yazyev, O.; Austin, A. J.; Cammi, R.; Pomelli, C.; Ochterski, J. W.; Ayala, P. Y.; Morokuma, K.; Voth, G. A.; Salvador, P.; Dannenberg, J. J.; Zakrzewski, V. G.; Dapprich, S.; Daniels, A. D.; Strain, M. C.; Farkas, O.; Malick, D. K.; Rabuck, A. D.; Raghavachari, K.; Foresman, J. B.; Ortiz, J. V.; Cui, Q.; Baboul, A. G.; Clifford, S.; Cioslowski, J.; Stefanov, B. B.; Liu, G.; Liashenko, A.; Piskorz, P.; Komaromi, I.; Martin, R. L.; Fox, D. J.; Keith, T.; Al-Laham, M. A.; Peng, C. Y.; Nanayakkara, A.; Challacombe, M.; Gill, P. M. W.; Johnson, B.; Chen, W.; Wong, M. W.; Gonzalez, C.; Pople, J. A. *Gaussian 03*, revision A.1; Gaussian, Inc.: Pittsburgh, PA, 2003.
- (43) Schmidt, M. W.; Baldridge, K. K.; Boatz, J. A.; Elbert, S. T.; Gordon, M. S.; Jensen, J. H.; Koseki, S.; Matsunaga, N.; Nguyen, K. A.; Su, S. J.; Windus, T. L.; Dupuis, M.; Montgomery, J. A. General atomic and molecular electronic-structure system. *J. Comput. Chem.* **1993**, *14*, 1347–1380.
- (44) (a) Zhan, C.-G.; Bentley, J.; Chipman, D. M. Volume polarization in reaction field theory. *J. Chem. Phys.* **1998**, *108*, 177–192. (b) Zhan, C.-G.; Chipman, D. M. Cavity size in reaction field theory. *J. Chem. Phys.* **1998**, *109*, 10543–10558. (c) Zhan, C.-G.; Chipman, D. M. Reaction field effects on nitrogen shielding. *J. Chem. Phys.* **1999**, *110*, 1611–1622.
- (45) (a) Zhan, C.-G.; Zheng, F. First computational evidence for a critical bridging hydroxide ion in phosphodiesterase active site. *J. Am. Chem. Soc.* **2001**, *123*, 2835–2838. (b) Zheng, F.; Zhan, C.-G.; Ornstein, R. L. Theoretical determination of two structural forms of the active site in cadmium-substituted phosphotriesterase. *J. Phys. Chem. B* **2002**, *106*, 717–722. (c) Zhan, C.-G.; Dixon, D. A.; Sabri, M. I.; Kim, M.-S.; Spencer, P. S. Theoretical determination of chromophores in the chromogenic effects of neurotoxicants. *J. Am. Chem. Soc.* **2002**, *124*, 2744–2752. (d) Dixon, D. A.; Feller, D.; Zhan, C.-G.; Francisco, S. F. Decomposition pathways of peroxytrinitro acid: Gas-phase and solution energetics. *J. Phys. Chem. A* **2002**, *106*, 3191–3196. (e) Dixon, D. A.; Feller, D.; Zhan, C.-G.; Francisco, S. F. The gas and solution phase acidities of HNO, HOONO, HONO, and HONO<sub>2</sub>. *Int. J. Mass Spectrom.* **2003**, *227*, 421–438. (f) Zhan, C.-G.; Dixon, D. A.; Spencer, P. S. Computational insights into the chemical structures and mechanisms of the chromogenic and neurotoxic effects of aromatic  $\gamma$ -diketones. *J. Phys. Chem. B* **2003**, *107*, 2853–2861.
- (46) (a) Chen, X.; Zhan, C.-G. Fundamental reaction pathways and free energy barriers for ester hydrolysis of intracellular second messenger 3',5'-cyclic nucleotide. *J. Phys. Chem. A* **2004**, *108*, 3789–3797. (b) Chen, X.; Zhan, C.-G. Theoretical determination of activation free energies for alkaline hydrolysis of cyclic and acyclic phosphodiester in aqueous solution. *J. Phys. Chem. A* **2004**, *108*, 6407–6413. (c) Zhan, C.-G.; Spencer, P. S.; Dixon, D. A. Chromogenic and neurotoxic effects of aliphatic  $\gamma$ -diketone: Computational insights into the molecular structures and mechanism. *J. Phys. Chem. B* **2004**, *108*, 6098–6104.
- (47) Tomasi, J.; Persico, M. Molecular interactions in solution: An overview of methods based on continuum distributions of solvent. *Chem. Rev.* **1994**, *94*, 2027–2094.
- (48) Mejias, J. A.; Lago, S. Calculation of the absolute hydration enthalpy and free energy of H<sup>+</sup> and OH<sup>-</sup>. *J. Chem. Phys.* **2000**, *113*, 7306–7316.
- (49) Cramer, C. J.; Truhlar, D. G. In *Solvent Effects and Chemical Reactions*; Tapia, O., Bertran, J., Eds.; Kluwer: Dordrecht, The Netherlands, 1996; p 1.
- (50) Chipman, D. M. Reaction field treatment of charge penetration. *J. Chem. Phys.* **2000**, *112*, 5558–5565.
- (51) Barone, V.; Cossi, M.; Tomasi, J. A new definition of cavities for the computation of solvation free energies by the polarizable continuum mode. *J. Chem. Phys.* **1997**, *107*, 3210–3221.
- (52) Tomasi, J.; Mennucci, B.; Cancès, E. The IEF version of the PCM solvation method: An overview of a new method addressed to study molecular solutes at the QM *ab initio* level. *J. Mol. Struct.: THEOCHEM* **1999**, *464*, 211–226.

- (53) Cancès, E.; Mennucci, B. Comment on “reaction field treatment of charge penetration”. *J. Chem. Phys.* **2001**, *114*, 4744–4745.
- (54) Cossi, M.; Rega, N.; Scalmani, G.; Barone, V. Polarizable dielectric model of solvation with inclusion of charge penetration effects. *J. Chem. Phys.* **2001**, *114*, 5691–5701.
- (55) Chipman, D. M. Energy correction to simulation of volume polarization in reaction field theory. *J. Chem. Phys.* **2002**, *116*, 10129–10138.
- (56) Tawa, G. J.; Topol, I. A.; Burt, S. K.; Caldwell, R. A.; Rashin, A. A. Calculation of the aqueous solvation free energy of the proton. *J. Chem. Phys.* **1998**, *109*, 4852–4863.
- (57) Topol, I. A.; Tawa, G. J.; Burt, S. K.; Rashin, A. A. On the structure and thermodynamics of solvated monoatomic ions using a hybrid solvation model. *J. Chem. Phys.* **1999**, *111*, 10998–11014.
- (58) Zhan, C.-G.; Dixon, D. A. Absolute hydration free energy of the proton from first-principles electronic structure calculations. *J. Phys. Chem. A* **2001**, *105*, 11534–11540.
- (59) Zhan, C.-G.; Dixon, D. A. First-principles determination of absolute hydration free energy of hydroxide ion. *J. Phys. Chem. A* **2002**, *106*, 9737–9744.
- (60) Zhan, C.-G.; Dixon, D. A. The nature and absolute hydration free energy of the solvated electron in water. *J. Phys. Chem. B* **2003**, *107*, 4403–4417.
- (61) Zhan, C.-G.; Dixon, D. A. Hydration of the fluoride anion: Structures and absolute hydration free energy from first-principles electronic structure calculations. *J. Phys. Chem. A* **2004**, *108*, 2020–2029.
- (62) Morris, G. M.; Goodsell, D. S.; Halliday, R. S.; Huey, R.; Hart, W. E.; Belew, R. K.; Olson, A. J. Automated docking using a Lamarckian genetic algorithm and empirical binding free energy function. *J. Comput. Chem.* **1998**, *19*, 1639–1662.
- (63) Solis, F. J.; Wets, R. J. B. Minimization by random search techniques. *Math. Oper. Res.* **1981**, *6*, 19–30.
- (64) Mehler, E. L.; Solmajer, T. Electrostatic effects in proteins: comparison of dielectric and charge models. *Protein Eng.* **1991**, *4*, 903–910.
- (65) Gao, F.; Bren, N.; Burghardt, T. P.; Hansen, S.; Henchman, R. H.; Taylor, P.; McCammon, J. A.; Sine, S. M. Agonist-mediated conformational changes in acetylcholine-binding protein revealed by simulation and intrinsic tryptophan fluorescence. *J. Biol. Chem.* **2005**, *280*, 8443–8451.
- (66) (a) Henchman, R. H.; Wang, H.-L.; Sine, S. M.; Taylor, P.; McCammon, J. A. Asymmetric structural motions of the homomeric  $\alpha 7$  nicotinic receptor ligand binding domain revealed by molecular dynamics simulation. *Biophys. J.* **2003**, *85*, 3007–3018. (b) Henchman, R. H.; Wang, H.-L.; Sine, S. M.; Taylor, P.; McCammon, J. A. Ligand-induced conformational change in the  $\alpha 7$  nicotinic receptor ligand binding domain. *Biophys. J.* **2005**, *88*, 2564–2576. (c) Law, R. J.; Henchman, R. H.; McCammon, J. A. A gating mechanism proposed from a simulation of a human  $\alpha 7$  nicotinic acetylcholine receptor. *Proc. Natl. Acad. Sci. U.S.A.* **2005**, *102* (19), 6813–6818. (d) Taly, A.; Delarue, M.; Grutter, T.; Nilges, M.; Novère, N. L.; Corringer, P. J.; Changeux, J. P. Normal mode analysis suggests a quaternary twist model for the nicotinic receptor gating mechanism. *Biophys. J.* **2005**, *88*, 3954–3965.

JM0606701